Compact, Robust Technology for Next-Generation Ultrafast High-Power Fiber Lasers

by

Matthew A. Rever

A dissertation submitted in partial fulfillment
of the requirements for the degree of
Doctor of Philosophy
(Electrical Engineering)
in The University of Michigan
2010

Doctoral Committee:

        Professor Almantas Galvanauskas, Chair
        Professor Karl M. Krushelnick
        Professor Theodore B. Norris
        Professor Herbert G. Winful

To Monica and my family

ACKNOWLEDGEMENTS

Coming up with a comprehensive acknowledgment list is a difficult if not impossible task, but I'll do my best. Of course, I need to thank my advisor, Professor Almantas Galvanauskas, first, for giving me the opportunity to work on such a rewarding project and for taking me on when I had already been in grad school for so long. Whenever it seemed like an experiment wasn't going to work, he always found a way to either make it work or to turn the negative result into something interesting in and of itself. I also need to thank the rest of my committee, Professors Herb Winful, Ted Norris, and Karl Krushelnick, for taking time out of their extremely busy schedules to read my dissertation, attend my defense, and provide insightful feedback to improve the quality. I'd also like to thank Professors Norris and Winful for teaching some of the most useful classes I've ever taken.

Nearly all of the results in my thesis revolved around the volume Bragg gratings developed by Doctors Vadim Smirnov and Leonid Glebov and their respective teams. This thesis would not have been possible without their work and insight.

Grad school would not have been nearly as productive and enjoyable without having great colleagues to work with. Special thanks to Dr. Shenghong Huang, who worked with me during the power scaling experiments that produced the most useful data presented here. I can't imagine how incredibly difficult it would have been to do the work without his tirelessly operating and maintaining the amplifiers no matter how long the hours and how many times something went wrong. I wish him the

Bixue Hou for doing the X-ray experiments with me, and special thanks to John for giving me my first lab experience and for being the general "go-to" guy at CUOS.

All these people so far, and I haven't even covered members of my first group yet, which I was in for more than half my time in grad school. Listing them all would double the length of my acknowledgments section, so I'd just like to give a big thanks to Dr. Scott Sepke for not only getting but also laughing at my constant barrage of Simpsons references (and for making his own), and for being a sounding board when I had to make some difficult decisions, which subsequently resulted in his taking some flak himself. And as for everyone else, most of whom I parted on good terms with and a few I didn't, I'll always remember the good times, and I wish everyone the best.

My family has been a constant source of support throughout all the years. I'd like to thank my mother, father, step-father, aunts, great-aunt, uncles, grandmother, sister, and everyone else for always being there, and for not giving me too hard of a time for taking so long. I love you all. And special thanks to my mother and step-father for always being there when I needed help with something.

And thanks to all my other friends over the years who made life infinitely more enjoyable; so many to name but they all know who they are...

Last and far from least, my girlfriend Monica, who has been with me since undergrad and has shown unlimited caring, understanding, and patience throughout the years. Words cannot begin to express my love and gratitude.

TABLE OF CONTENTS

LIST OF TABLES

LIST OF FIGURES

CHAPTER I

Introduction

Optical chirped-pulse-amplification (CPA), a means of generating energetic ultrashort pulses by lengthening the pulses prior to amplification [4], has ushered in a new era for physics research and industrial applications. The high fields generated by tightly focusing these high peak power pulses enable the study of matter under extreme conditions. As a result, novel sources for X-ray, gamma-ray, electron, and proton beams are being developed [5]. Attosecond pulses useful for fundamental chemistry and biology research have been generated [6]. Moreover, exciting applications such as terahertz and extreme ultraviolet generation, as well as materials inspection and processing are made possible [7, 8, 9].

Though the applications of CPA span a broad range and are potentially revolutionary, ultrafast laser systems are still somewhat limited in terms of usage due to their current level of practicality. Conventional bulk solid-state lasers, such as those based on Ti:Sapphire or Nd:Glass, are the current workhorses of the ultrafast community. These technologies have yielded extremely short (sub-ps to few-fs) pulses with very high energies (mJ to kJ and beyond) and have demonstrated the potential for ultrahigh peak-power lasers. However, these systems are quite large, often requiring multiple optical tables or even several rooms. Furthermore, there are

many free-space optics present, each requiring delicate alignment that can easily deteriorate over fairly short periods of time due to vibrations, thermal drift, imperfect opto-mechanics, etc. As a result, these bulk lasers are not usable in places where space is at a premium or in inhospitable environments such as manufacturing facilities or mobile laboratories. And reliability is another major issue, as the complex realignment requires highly-trained technicians or engineers on hand and can result in substantial down-time.

Another drawback of these bulk solid-state lasers is their power scalability. Applications such as materials processing benefit tremendously from high average powers as the processing times are reduced in proportion resulting in greater productivity [9]. For processes such as THz and attosecond generation, where the conversion efficiencies are very low (a small fraction of a percent) [10, 11], high average powers are critical for timely and thorough investigations. Ti:Sapphire crystals, even with their high thermal conductivities and sophisticated cryogenic-cooling systems, are still limited in power scalability to the tens of Watts level due to the formation of thermal aberrations and are subject to damage at greater power levels. A clever workaround to this issue has been the use of thin-disk crystal geometries which mitigate the thermal effects on the beam due to the quasi-longitudinal heat-dissipation [12]. Though high average powers have been obtained [13] from these systems, they still suffer from limited compactness and robustness due to their bulk amplifier configurations.

What is then needed is a gain medium that can be made with a compact geometry in a robust, alignment-free configuration. As well, the medium needs to be scalable in power without suffering from thermal degradation. Clearly, rare-earth (Yb, Er) doped fiber amplifiers meet the criteria. Many meters of fiber length can be coiled into a small package. The fiber ends can be spliced together and onto monolith-

ically integrated components. Fibers have a large surface-to-volume ratio thereby increasing cooling efficacy. Yb-amplifiers have a very low ($< 10\%$) quantum defect, allowing for pump-signal slope-efficiencies exceeding 80%. And the output mode is determined by the waveguide structure of the fiber and therefore will not suffer from thermal aberrations at high power.

Fiber amplifiers have been shown to provide robust operation up to the multi-kW level in CW mode [14]. Millijoule energies have been obtained for long-pulse operation while maintaining sufficient Raman and Brillouin suppression [15]. CPA operation has even been demonstrated at nearly a kW (800 W) [16] for 10 μJ energies and nearly a mJ [17] at a 100 kHz repetition rate (100W average power).

While the potential for fiber lasers is clearly indicated, several issues remain for ultrafast fiber-CPA systems to reach their potential. Firstly, fiber-CPA systems still rely on conventional bulk diffraction-grating-based stretchers and compressors. These are large devices that require intricate alignment that offset the benefits of compactness and robustness for fiber lasers. Secondly, the mode-field-diameters (MFDs) of fibers are on the order of a few to a few tens of μm, and the amplifier lengths are on the order of meters. The result is a relatively high-intensity pulse propagating over a large distance, causing the build-up of nonlinear phase which degrades the recompressed pulse quality. Clearly, larger MFDs are needed to reduce this nonlinear effect. However, simply increasing the fibers core diameter increases the number of modes that can propagate. This is deleterious for any fiber system, as the output beam will deviate further from the diffraction limit as more modes are present. It is devastating for a CPA system, as not only will the spatial quality degrade, but the energy will spread throughout the modes which propagate at different group velocities, resulting in a broad temporal spread after recompression.

Solutions to these problems will hence be proposed and demonstrated.

1.1   Chirped Volume Bragg Gratings

Chirped fiber Bragg Gratings have long been used for dispersion compensation as well as stretchers and compressors for fiber-CPA [18]. As they are fiber devices themselves, they obviously satisfy the criteria of small-size and monolithic integration making them compatible with the benefits of fiber lasers. And they are capable of stretching pulses to hundreds of ps or more. However, they are still limited in terms of energy scaling to sub-μJ levels due to their small core sizes. Dispersion-engineered photonic crystal fibers suffer from the same problem.

What is needed then is a device similar to a fiber grating but has a much larger transverse size, namely several millimeters to several centimeters across. Chirped volume Bragg gratings, devices that operate on the same principle as their fiber counterparts but are written in bulk glass, are the solution. The development of photo-thermo-refractive (PTR) glass has enabled the writing of periodic or quasi-periodic (i.e. linearly varying) Bragg structures onto glass of centimeter dimensions with nearly uniform transverse index modulation via exposure to a UV laser inter-ference pattern [19]. Figure 1.1 illustrates the principle of CVBG operation. In only a few centimeters of length (the chirp-rate is 100 ps/cm assuming a group index 1.5 and taking into account the double-pass effect when computing the group delay dif-ference between the shortest and longest wavelengths), an ultrashort pulse can be stretched to hundreds of picoseconds and can be recompressed simply by launching it into the opposite end. The transverse dimensions allow for recompression of mJ energy pulses [20]. And since the alignment is simple, they can be engineered for robust, monolithic integration into a fiber system with a minimal footprint.
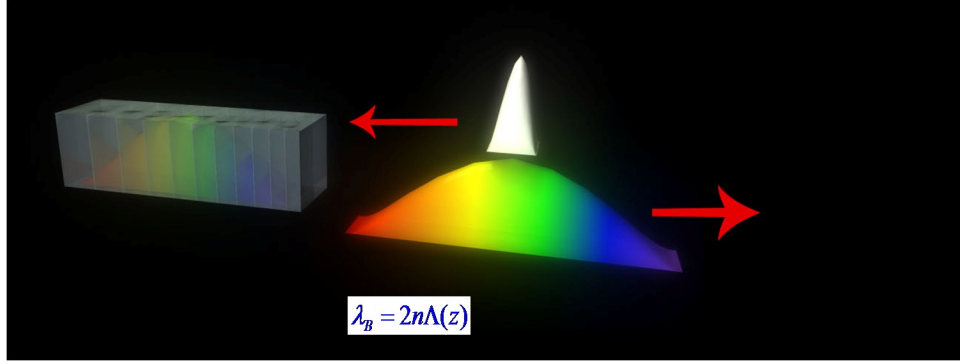
Figure 1.1: Illustration of the principle of CVBG operation
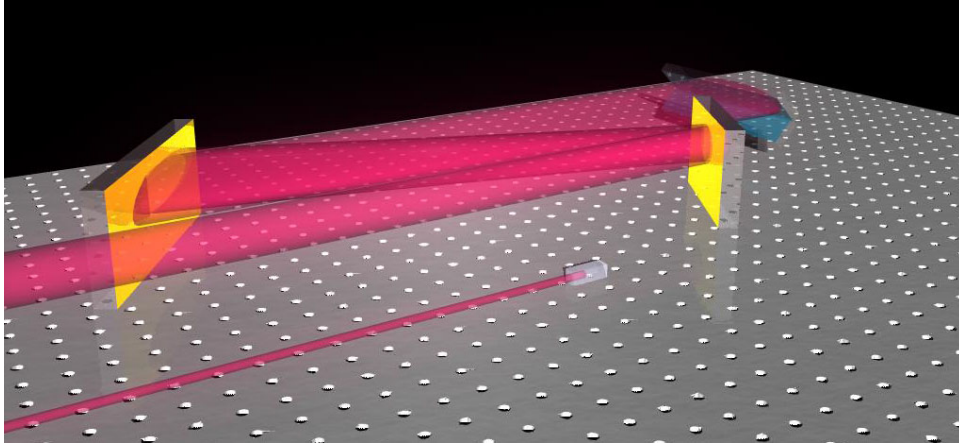
Figure 1.2: Comparison of a CVBG compressor to a conventional bulk diffraction grating compressor

To have an accurate idea of how advantageous a CVBG device is to a typical Treacy-type bulk grating compressor [21], Figure 1.2 shows an illustrative comparison of the two. As can be seen, the CVBG is much simpler and smaller. Furthermore, it must be taken into account that each of the gratings in the Treacy compressor must be precisely aligned and positioned in three dimensions, and there would be even more degrees of freedom for a reciprocally positively chirped stretcher (such as a Martinez [22] or Offner type) where positive lenses or mirrors are used to image the beams. A summary of the advantages of CVBGs over their alternatives is presented in Table 1.1.

The efficacy of CVBGs for fiber-CPA is the main topic of this thesis. Multiple

issues are addressed to demonstrate the potential of this new technology. Chapter III presents an experimental demonstration of the power handling capabilities of CVBG compressors to hundreds of Watts and also shows that spatial-chirp-free gratings can be written for broad-bandwidths. Chapter IV presents an analysis that explains the physical processes that degrade the dispersion characteristics of CVBGs at high power due to non-uniform thermal loading. The potential for kW scaling is explored. Chapter V analyzes the temporal reciprocity (the temporal fidelity after stretching and compressing with the same CVBG) of the devices over their parameter space and shows that CVBGs are indeed robust for ultrafast fiber-CPA. Energy scaling with CVBGs is demonstrated in Chapter VI.

1.2 Robustly Single-mode Chirally-Coupled-Core Fibers

The most obviously way to decrease nonlinearity in an optical fiber is to simply increase the core size. The caveat, of course, is the characteristic V parameter increases linearly with the core diameter, and when $V \gg 2.405$, many transverse modes are allowed to propagate. Consequently, the output beams will not be diffraction-limited and intermodal dispersion will broaden the pulse temporal profiles. It is possible to obtain single-mode operation in multimode fibers with careful input coupling [23] as well as coiling the fibers so as to preferentially attenuate the higher-order modes [24].

	Chirped Volume Bragg Grating	Diffraction Grating Pair	Chirped Fiber Bragg Grating Pair	Hollow Core-Photonic Crystal Fiber
Energy	Scalable	Scalable	$\ll 1~\mu J$	$\sim 1~\mu J$
Average Power	>100 W	R:$\sim$10 W T:>100 W	$\sim$1 W	$\sim$100 W
Stretched pulse	Long ($\sim$ns)	Long	Long	Short ($\sim$ps)
Compact/robust	Yes	No	Yes	Yes
Polarization sensitivity	No	Yes	No	No

Table 1.1: Stretcher/Compressor Comparison

Indeed, single-mode operation has been demonstrated in large-mode area (LMA) fibers with core sizes as large at 65 μm in diameter operating at Yb wavelengths (1064 nm) [25]. However, at core diameters about 20 μm, single-mode operation becomes highly sensitive to any perturbation and therefore lacks robustness. Splicing is possible, but an extremely high degree of precision is necessary and is generally impractical.

Multiple novel technologies have been proposed to overcome this limitation. Generally, the concept is to increase the effective mode area while only allowing only one mode to propagate. A technology that has garnered significant attention in recent years has been photonic-crystal-fibers (PCFs) [26]. These guide light in a nanostructered core with holes in the cladding. Up to 100 μm core diameters have been demonstrated with (quasi-) single-mode operation at 1040 nm [27], which has allowed for mJ energy scaling at 100 kHz operation resulting in 100 W of output power in sub-ps CPA mode [17]. Though PCFs are attractive for their power handling capabilities, they do not maintain all of the advantages of fiber systems. Firstly, at larger core diameters (> 40 μm), it is necessary to make the cladding rigid. This increases the required size of the amplifier, as roughly 1 m is necessary for sufficient pump absorption (the pump absorption is 30 dB/m) and signal gain [28], offsetting system compactness. Moreover, due to the nature of the fine structure, splicing is generally not feasible, thereby introducing a requirement for free-space coupling and therefore offsetting system robustness.

Another competing technology is leakage-channel-fibers (LCFs) in which single-mode operation is achieved by surrounding a solid-core by a ring of air-holes that leak out the higher-order modes [29]. Effective mode-field diameters of up to 100 μm have been demonstrated [30, 31], and powers as high as 100 W has been achieved

with leakage-channel fiber amplifiers [32]. Similarly to PCF, LCFs are intriguing for power scaling but still suffer from limited robustness.

A novel idea for obtaining single-mode operation that does not involve microstructures is intentional higher-order mode (HOM) excitation in step-index large-mode area fibers [33]. The principle behind this is that the difference between the propagation constants of the modes becomes larger for higher modes, thereby reducing the coupling between them. As a result, quasi-single-mode operation becomes feasible. The main drawback to this technique is that it is generally more desirable to have fundamental LP_{01} mode (an almost Gaussian TEM_{00} beam) operation for its large effective mode-field diameter and for its free-space propagation and focusing properties.

Ideally, a fiber could be made with single-mode propagation in a large-mode area but still be coiled and spliced for compact, monolithic laser architectures. The concept used in this work is chirally-coupled-core (CCC) fibers, which are LMA fibers with a smaller helical side-core [34]. The side-core induces high HOM losses (tens of dB/m) with minimal perturbation of the fundamental mode. Figure 1.3 illustrates the CCC concept.

Previously, up to 310 W CW and 106 W pulses (1 mJ pulses at 100 kHz repetition) have been demonstrated [35, 15] with CCC fiber amplifiers with robust, single-mode operation. Core diameters up to 38 um have been manufactured with good fundamental-mode preservation and high HOM losses. References [35, 15] detail the operation of CCC fibers as well the progress. This work presents the first demonstration of CPA with CCC amplifiers. The experimental setup is discussed in Chapter III, and the results are critical for the analysis in Chapter IV.
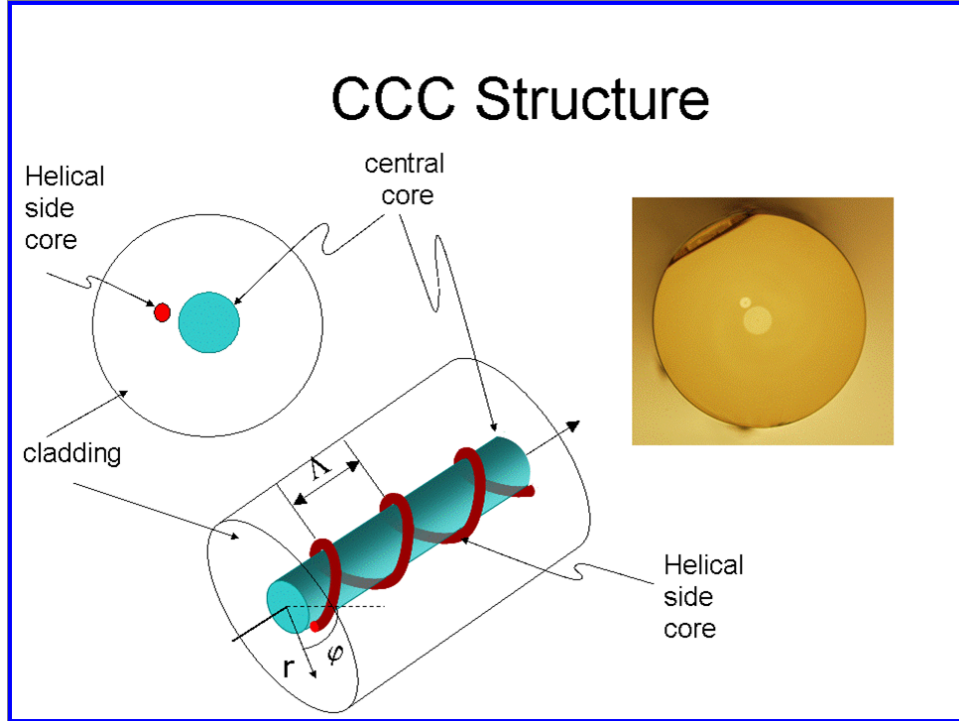
Figure 1.3: Concept of Chirally-Coupled-Core Fibers ; a helical side-core preferentially couples energy out of the higher-order modes, resulting in an effectively single-mode large-mode area fiber

1.3 Fiber CPA Energy Scaling and Applications

Of course, many CPA applications require high pulse energies, ranging from multi-uJ to mJ and beyond. Processes that require high field strengths such as X-ray, electron, and proton acceleration are examples where field strengths of 10^{15} W/cm^2 and higher are necessary, thereby requiring mJ energies with tight focal spots (few um) and short pulse durations ($\sim$100 fs). Since fiber amplifiers have small beam sizes propagating through long lengths of material by comparison to bulk solid-state amplifiers, fiber-CPA systems require substantially longer stretched pulse durations in order to mitigate the induced nonlinear phase, quantitatively characterized by the B-integral given in Equation 1.1.

$$(1.1) \qquad B = \frac{2\pi}{\lambda} \int n_2 I(z) dz,$$

where B is the total nonlinear phase, λ is the wavelength, n_2 is the nonlinear index, and I(z) is the pulse intensity along the fiber.

Generally, unless careful pulse shaping is employed (i.e. parabolic stretched pulses [36]), it is necessary to have a B-integral approximately π or less in order to have a recompressed pulse that is reasonably close to its transform limited computed by the zero-phase Fourier transform of its spectrum. This is primarily due to self-phase-modulation, which is shown to be the most deleterious effect for ultrafast fiber-CPA, more so than four-wave-mixing as well as Raman or Brillouin scattering. To provide a concrete example, consider a fiber amplifier of 3 m in length with 30 dB of gain, assuming uniform inversion (and hence gain-coefficient) with no saturation effects (simple exponential-gain) with an effective mode-field-diameter of 30 μm. Let the final output energy be 10 μJ. Equation 1.1 can be computed simply by noting that with exponential gain, the integration over z results in an effective length given by Equation 1.2:

$$(1.2) \qquad z_{eff} = \frac{1 - e^{-gL}}{g},$$

where zeff is the effective length, g is the amplifier gain, and L is the physical length.

The total nonlinear phase, or B-integral, is then:

$$(1.3) \qquad B = \gamma z_{eff} P_0$$

with

$$(1.4) \qquad \gamma = \frac{n_2 \omega_0}{c A_{eff}}$$

where P$_0$ is the final output power, ω_0 is the optical angular frequency, c is the speed of light, and A$_{eff}$ is the effective mode area. Solving for B=π, a stretched pulse duration of 350 ps is found to be necessary.

Limpert et al have demonstrated mJ fiber-CPA with 800 fs recompressed pulse durations [17]. However, this was accomplished using bulk diffraction-grating stretchers and compressors that greatly increased the size of their setup to several meters in length. CVBG-based stretchers and compressors have been used to obtain ~mJ level pulses in bulk solid-state CPA systems [20], indicating that nonlinear Kerr effects such as SPM and self-focusing are not detrimental at these energy levels for the current generation of CVBGs of several centimeters in length and ~0.5 cm transverse dimensions.

Indeed, a simple argument can be made to show that the nonlinear phase in a fiber amplifier will be much greater than that in the CVBG compressor. Consider that the stretching factor in a fiber-CPA system is approximately 1000 (for instance, stretching 300 fs to 300 ps). The ratio of the mode-field diameter in the CVBG is about 3 mm for current gratings, whereas it is about 30 μm in an LMA fiber. This yields an area ratio of 10,000. Even under the unrealistically worst case scenario of having the transform-limited pulse propagating throughout the entire double-pass length of a current CVBG, which is 6 cm, and taking a typical amplifier effective length of 1 m, the ratio of nonlinearity in the CVBG compressor to the fiber amplifier is (1000/10000)x(0.06/1) = 0.006. Therefore, the nonlinearity of the CVBG compressor will not be the limiting factor for energy scaling.

In this work, CVBG-based stretchers and compressors are used to scale the energy in an Yb-fiber CPA system. Chapter VI describes the experiment and the measured results. To demonstrate the viability of fiber-CPA for high-field applications, X-

ray generation via multi-μJ, few hundred femtosecond pulses from a fiber-CPA laser interacting with a solid target without a vacuum-chamber is presented in Chapter VII.

CHAPTER II

Background

As the majority of the results presented in this thesis center around Chirped Volume Bragg Gratings (CVBGs), it is important to first establish a background to put the current research issues in context. This chapter will present an overview of CVBG technology. Section 2.1 will cover the essential material properties of photo-thermo refractive (PTR) glass, the material that comprises CVBGs. A knowledge of the material properties will be essential to analyzing the thermal properties, the major topics of Chapters III and IV, as well as understanding fabrication limitations and damage thresholds which determine the range of parameters in which the devices can safely operate. Section 2.2 discusses the process for writing the CVBGs in PTR glass. A major issue blocking the widespread usage of CVBGs has been the presence of spatial chirp, in which the different wavelength components of the incident beam are reflected at different angles, resulting in degraded beam quality and a narrowing of the spectrum being coupled into a fiber (after the stretcher particularly). Examining the CVBG fabrication process will allow for an understanding of the origin of the spatial chirp, how to quantify it, and most importantly, how to eliminate it. Progress in CVBG fabrication leading up to the current generation of broadband, spatial chirp-free CVBGs will be presented.

Furthermore, once the fundamental physical properties of CVBGs are known, their operation as ultrashort pulse stretchers and compressors must be understood at a quantitative level. Section 2.3 discusses the physics of Bragg reflection, which will lead to the development of mathematical models that compute the spectral response, both magnitude and phase, of Bragg gratings. Then the models can be applied to long Bragg gratings with a linear chirp, due to a linear varying spatial period. It will be shown that there is a ripple present in both the profile and phase of the spectral response, which will cause a deleterious effect on the recompressed pulses. This effect will be quantified theoretically and experimentally in Chapter V.

Lastly, as Chirally Coupled Core (CCC) fiber amplifiers are critical to the power scaling results in this thesis, the basic pronciple governing their operation is examined in Section 2.4.

2.1 Photo-thermo Refractive Glass Properties

Given the numerous attractive properties of Chirped Volume Bragg Grating (CVBG) based stretchers and compressors described in Chapter I and their relatively simple concept, the question naturally arises as to why this technology has only become feasible in recent years. Indeed, attempts were made over a decade ago to fabricate CVBGs (and volume Bragg gratings (VBGs) in general) using various materials. The most prolific example of a material for early VBG attempts is germano-silicate glass that is doped with hydrogen to make it photosensitive to ultraviolet (UV) radiation for device writing. Unfortunately, the UV aborption coefficient of greater than 100 dB/mm [37] made it impossible to write even modest size VBGs with quasi-uniform transverse index profiles, which are necessary for spatial and spectral beam fidelity. The transverse dimensions of the VBGs were limited to less than 0.5 mm as a result

of this very large absorption [38].

Alternatives to germano-silicate glass used for attempting fabrication of VBGs included photopolymers, photographic emulsions, dichromated gelatin, and photore-fractive crystals. None of these paterials proved practical for VBG laser applications, however, due to degradation via humidity, excessive sensitivity to ambient temper-ature, or shrinking after development. Moreover, the damage thresholds for laser pulses are quite low, thereby mitigating their usefulness in high average and peak power chirped-pulse-amplification systems.

Clearly, a robust material that has high damage thresholds and minimal sensi-tivity to ambient environmental conditions and that has a usable UV absorption coefficient is necessary to manufacture practial VBG devices. Fortunately, a ma-terial was discovered that possesses all of these properties, namely photo-thermo refractive (PTR) glass. PTR glass is a UV holographic recordable material that can be produced with bulk (centimeter) dimensions with excellent homogeneity and that has damage properties comparable to those of fused silica with even greater thermal conductivity [19]. As a result, CVBGs can be written in PTR glass that are capa-ble of operating at hundreds of Watts, as demonstrated in Chapter III and at ∼mJ energies, as demonstrated in Chapter VI.

To produce PTR glass, a sodium-zinc-aluminum-silicate glass is doped with flourine, silver, and cerium. The dopants are necessary for the photo-writing and develop-ment processes. It is the cerium Ce^{3+} ions that make the glass photosensitive to the UV radiation between 280 nm and 350 nm [39]. When the glass sample is exposed to UV radiation, the Ce^{3+} ions are stripped of an additional electron, resulting in Ce^{4+} ions. The ejected electrons are taken in by the silver Ag^+ ions thereby neu-tralizing their charge. This in itself does not modify the glass index of refraction,

but a higher density of neutral silver atoms will affect the refractive index after the thermal annealing treatment. This annealing process is performed by placing the PTR glass sample in an oven with an operating temperature of approximately 500 degrees Celsius. At this temperature, the neutral silver atoms are diffused which lead to the creation of silver nano-particles. The oven temperature is subsequently raised by 50 degrees Celsius. This allows for the crystaline phase precipitation for the NaF as the silver nano-particles act as nucleation centers. The sodium fluoride has a lower refractive index, n = 1.32, than the PTR glass, which has a refractive index n = 1.49. Depending on the NaF density, the PTR glass sample can have its index lowered on the order of 10^{-3} [46], which is more than sufficient to have Bragg gratings with well over 95% diffraction efficiencies for bandwidths of several nanometers or more. This new recorded index profile is stable under laser illumination and can safely withstand operating temperatures over 100 Kelvin beyond room temperature without degradation, which will be shown to be essential in the subsequent CVBG power scaling chapters.

Figure 2.1 shows the absorption spectra of the PTR glass. The absorption coefficient rises sharply at wavelengths below 350 nm and is large at wavelengths as short as 280 nm corresponding to the Ce^{3+} absorption spectrum. This window necessitates the use of lasers operating in the UV range for writing the gratings. PTR glass is nearly completely transparent (absorption coefficient of 10^{-2} or less betwwen 350 and 2700 nm, making it useful for a medium for volume Bragg gratings in the optical and near-infrared range in which the vast majority of chirped-pulse-amplification lasers operate.

Even in the UV range, the absorption coefficient is fairly small, on the order of 1 cm^{-1}. Since the absorption is exponentially decaying, this allows for the writing of
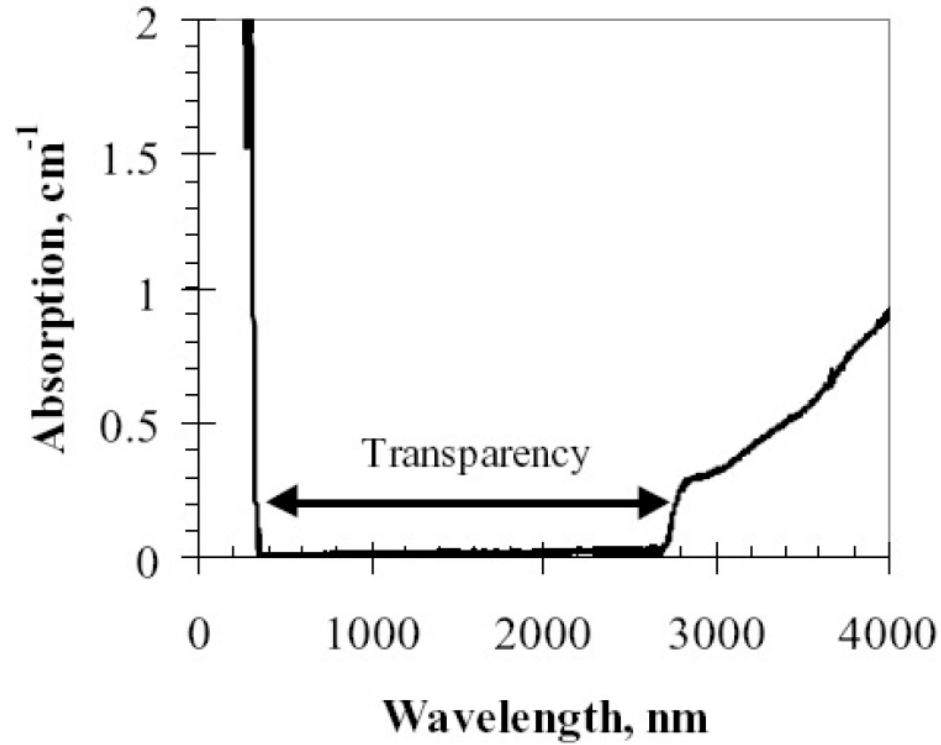
Figure 2.1: Absorption spectra of PTR glass

VBGs with centimeter scale transverse dimensions with a nearly uniform transverse refractive index profile, essential for preserving beam quality. A centimeter-scale transverse aperture allows for easy alignment into the VBG without having to down-collimate the beam and will allow for a beam area of 10,000 or greater than that in the fiber, mitigating nonlinear and damage effects.

2.2 Chirped Volume Bragg Grating Fabrication

In order to achieve the necessary holographic interference pattern corresponding to a chirped volume Bragg grating, i.e. quasi-planar transverse index profiles with a linearly increasing longitudinal index period, a Mach-Zender interfermeter is used. Figure 2.2 illustrates the interferometric setup. A laser with a wavelength in the UV range of 280-350 nm is clearly needed to seed the interferometer due to the
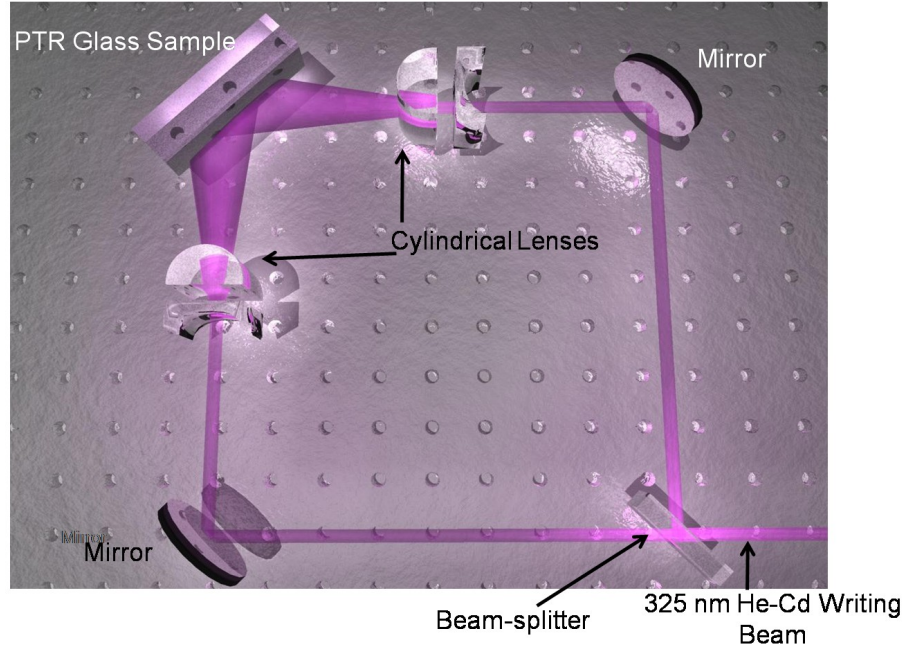
Figure 2.2: Chirped Volume Bragg Grating Mach-Zender interferometric writing setup

absorption range of the PTR glass. As the absorption coefficient decreases towards the longer wavelength side, larger transverse dimension gratings can be written if the wavelength is between ∼320 and 350 nm. Suitable candidates include He-Cd lasers, with a wavelength of 325 nm, N_2 lasers, with a wavelength of 337 nm, or Ar-ion lasers, with a wavelength of 351 nm. A He-Cd laser is the choice of the CVBG supplier for this work, OptiGrate Corp. located in Orlando, Florida.

The grating index pattern is created by the interference of the two diverging UV beams after the cylindrical lenses. Cylindrical lenses are used to create a longitudi-nally varying period but quasi-planar transverse profiles. The cross-angle of the two beams determines the central operating wavelength of the CVBG. The chirping rate is determined by the beams' divergences.

2.2.1   PTR Glass Damage Threshold

Undoubtedly, CVBG deployment in high-power and high-energy CPA systems will not be viable if the underlying PTR glass cannot withstand the incident laser pulses. As the absorption coefficient in the IR region is quite small (10^{-2} or less), damage due to average power is not expected. Up to 200 W of average power is demonstrated with a CVBG in Chapter III with no signs of damage, and moreover, up to 6 kW of average power has been demonstrated in a narrowband VBG used for beam combining without any observable damage [40] in a measurement performed by OptiGrate with an IPG laser.

Previous experimental tests conducted at the University of Michigan indicate that PTR glass is resilient to cw optical powers, and optical damage with cw beams should not be a problem. Indeed, focusing a 945 nm cw laser laser beam with a 300 μm spot size for 5 minutes showed no damage, indicating that the damage threshold is in excess of 700 kW/cm^2 [41].

High energy pulse damage thresholds have also been tested for the PTR glass surface. For unprocessed PTR glass, the threshold for 1ns duration pulses was found to be 30 J/m^2 and for a sample with a volume grating written on to it the threshold was 20 J/m^2 [42]. These measurements were performed at 1054 nm with a 700 μm spot size. The damage thresholds are on par with that of fused silica, which has a surface damage threshold of 40 J/m^2. Moreover, up to $\sim$1 mJ has been demonstrated on a CVBG compressor in a Yb:KYW CPA laser system [20]. The indication is that CVBGs are well suited for energy scaling applications.

Nonlinearity is also a major concern as self-phase-modulation as self-focusing due to the Kerr effect could seriously degrade the compressed pulse temporal profile and beam quality, respectively. Measurements indicate that the nonlinear index value for

PTR glass, n$_2$ is equal to 3.3×10^{-20} m^2/W for both unprocessed and written samples. Table 2.1 compares the damage thresholds and nonlinear coefficients for PTR glass and fused silica.

2.2.2 Spatial Chirp

Originally, the CVBG writing setup was a Mach-Zender interferometer with a cylindrical lens chain in one arm and a collimated beam in the other, as shown in Fig. 2.3. This resulted in a serious deleterious effect. Namely, the resulting planes of constant index, rather than being all parallel to the CVBG surface normal as they should be, would instead be 'fanned' across the length of the grating. As a result, the reflected beam would have spatial chirp, wherein each of the wavelength components would exit the CVBG at a different angle along one of the beam's transverse axes.

Figure 2.4 illustrates the deleterious spatial chirp effect. Clearly, the beam will be substantially degraded after it experiences this effect; M^2 will be increased thereby degrading the focal spot after the compressor. Moreover, after the stretcher of a fiber-CPA system, the beam must be coupled into a fiber. The spatial chirp will cause an irregular, wavelength-dependent focal spot at the input of the fiber core. As efficient single-mode coupling depends on precise mode-matching, the different wavelengths

Material	Damage Threshold (J/m^2) (for 1 ns pulses)	Nonlinear index (10^{-20} m^2/W)
Developed PTR Glass	20	3.3
Unprocessed PTR Glass	30	3.3
Fused Silica	40	3.0

Table 2.1: Damage threshold and nonlinear index comparison for processed and unprocessed PTR glass with fused silica for reference
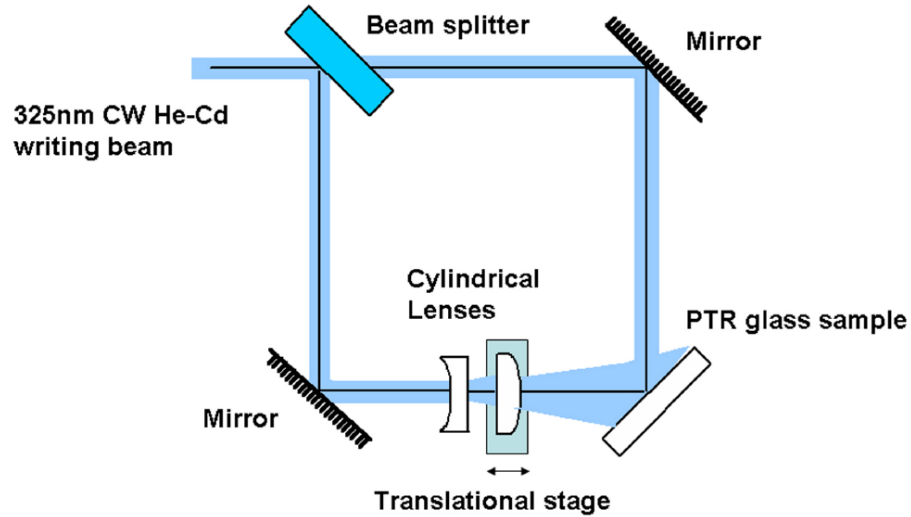
Figure 2.3: Original CVBG writing setup with cylindrical lenses in one arm only

will be coupled in with varying efficiencies, generally resulting in a spectral and corresponding power loss.

Much doubt has arisen as to the suitability of CVBGs for cutting-edge ultra-intense chirped pulse amplification lasers as a result of the first generation of gratings suffering from substantial chirp. Fortunately, this chirp is not an intrinsic effect. By introducing a second cylindrical lens system into the other arm of the Mach-Zender interferometer, as shown in Fig. 2.2, and by carefully designing the lenses for aberration correction, CVBGs that are spatial chirp free, within any measurement error, can be manufactured.

To quantify the spatial chirp, a measurement setup was constructed, shown in Fig. 2.5. The output of a tunable narrow-bandwidth ($\sim$0.2 nm) single-mode Yb-fiber laser (Littrow configuration) is injected into the CVBG under test at normal incidence. Due to the polarization independence of the CVBGs, a simple quarter waveplate and polarizing beam splitter can be used to inject the beam with circular polarization and convert it into an orthogonally polarized beam (with respect to
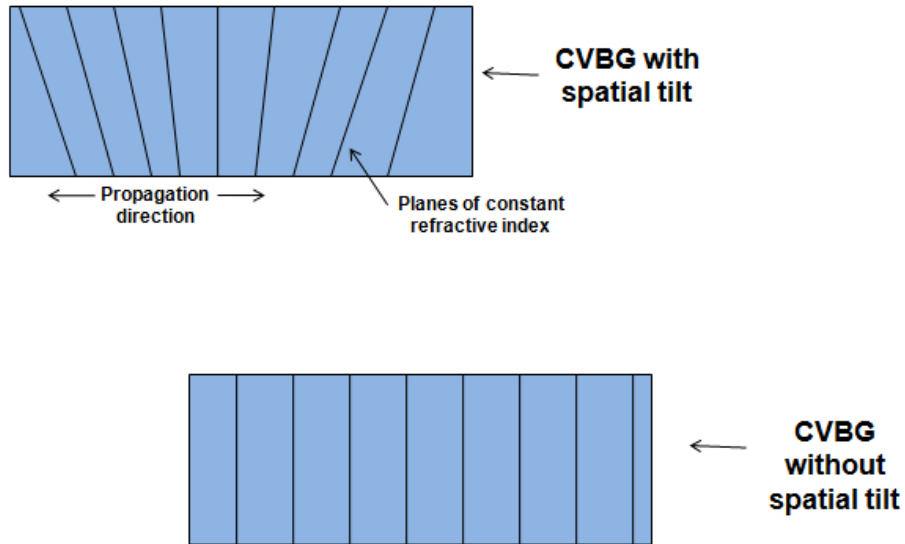
Figure 2.4: A chirped volume Bragg grating with and without spatial chirp
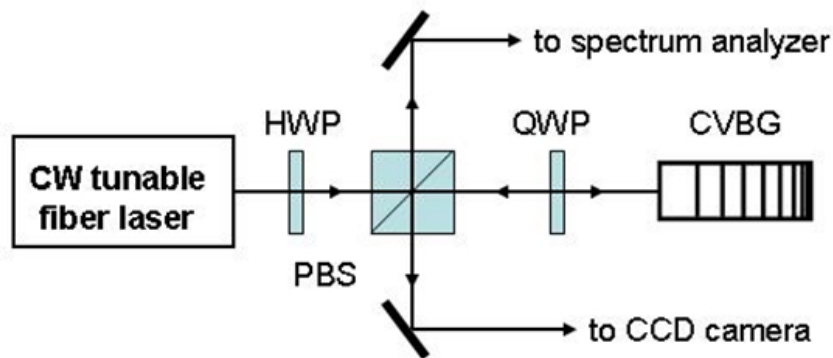
Figure 2.5: CVBG spatial chirp measurement setup; the chirp angle is measured by dividing the centroid shift on the CCD by the distance from the grating to the camera

the input polarization) to be redirected by the beam splitter. Hence, CVBGs can be operated at normal incidence with a trivially simple setup. The output beam is allowed to propagate for a distance of approximately 1 meter before it is incident on a CCD camera. By measuring the beam centroid shift as a function of wavelength, and dividing the shift by the distance between the CCD and the grating, the spatial chirp angle versus wavelength data is obtained.

By measuring the spatial chirp of the first generation chirped gratings and comparing the data to that of the second generation chirp-free gratings, it can be established
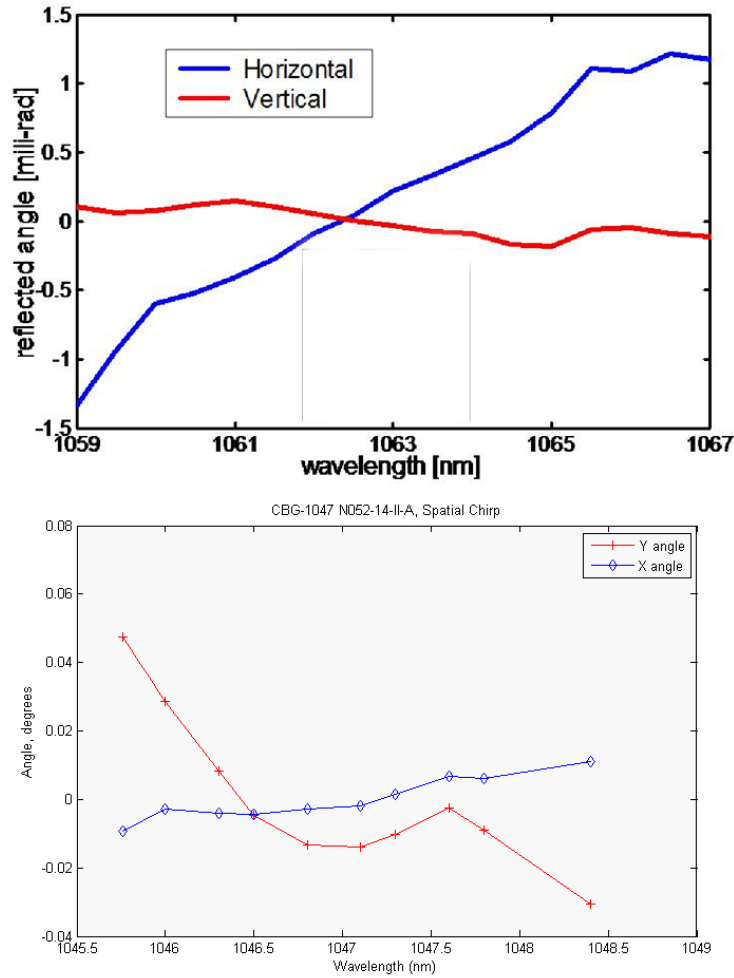
Figure 2.6: Spatial chirp measurements from first generation CVBGs

that the dual-cylindrical beam interferometric writing technique indeed makes the chirp neglegible for practical use. Figure 2.6 shows the spatial chirp measurements of first generation CVBGs of various bandwidths of between 2 and 3 cm in length suffering from a substantial amount of chirp. This can be compared to the data plotted in Fig. 2.7 corresponding to the second generation gratings with the improved writing apparatus. As can be seen, the chirp is reduced to a level beneath the noise floor of the measurement setup.

As further evidence, Fig. 2.8 contains false-color beam profile measurements from
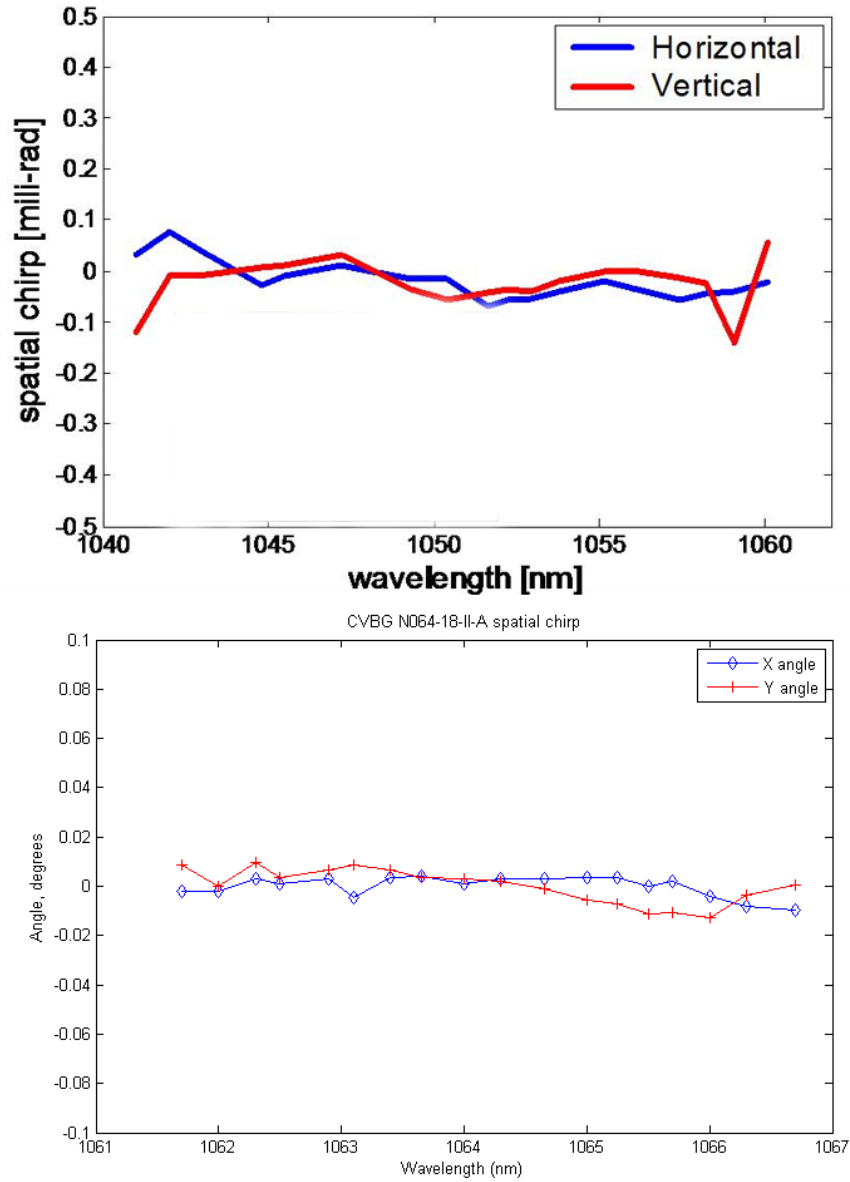
Figure 2.7: Spatial chirp measurements from improved second generation CVBGs. The plots are flat within experimental error.
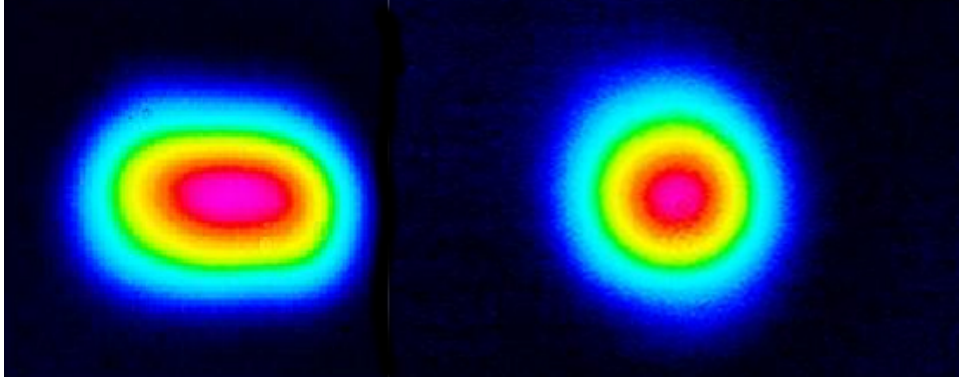
Figure 2.8: Reflected beam profiles from CVBGs with (left) and without (right) spatial chirp

a broadband, 10 nm bandwidth modelocked Nd:Glass laser (centered at 1064 nm) producing a train of 110 fs pulses at a repetition rate of 72 MHz incident on CVBGs of various bandwidths with (left) and without (right) spatial chirp. Clearly, the distortion from the first generation of gratings is noticeable, whereas it is insignificant for the newer enhanced CVBGs.

Most notable amongst the gratings measured is the second generation 27 nm bandwidth grating. The lack of spatial chirp in this broad-bandwidth CVBG indicates the high potential for CVBG-based stretchers and compressors for fiber-CPA lasers.

2.3 Bragg Reflection and Chirped Bragg Grating Models

At its core, a chirped volume Bragg grating is simply a thick dielectric stack of layers of alternating indices of refraction. Fiber Bragg gratings have long been used both for narrow-band high reflectors and for broadband applications in a chirped configuration, typically used to compensate the material and waveguide dispersion in the long (kilometer) lengths of fiber. A volume Bragg grating operates on the same principle of Bragg reflection, however, rather than have the light be guided in a waveguide, it propagates in a structure with broad (millimeter to centimeter) transverse dimensions that has no waveguide effect. The advantage is obvious; the

small mode size in the fiber limits the maximum energy to sub-μJ levels in order to prevent damage or excessive nonlinearity, i.e. self-phase-modulation, four-wave mixing, or stimulated Raman or Brillouin scattering, wherein a CVBG is scalable to the mJ level without suffering from these effects.

Figure 2.9 presents a graphical representation of a volume Bragg grating structure. The index of refraction is governed by the following equation:

$$(2.1) \qquad n(x, y, z) = \begin{cases} n_2, & 0 \leq z \leq \Lambda/2 \\ n_1, & \Lambda/2 < z < 0 \end{cases}$$

where z is the normal grating axis. As the structure is longitudinally periodic, the index must satisfy the relationship:

$$(2.2) \qquad n(x, y, z) = n(x, y, z + \Lambda)$$

where Λ is the fundamental VBG period. The index is uniform across the transverse coordinates x and y where x and y are less than or equal to the width and height, respectively, of the grating.

Reflection occurs due to constructive interference of the backward reflecting waves caused by Fresnel reflections at the index of refraction discontinuity interfaces. The wave vector components are given by the equations

$$(2.3) \qquad k_x = \frac{2 * \pi * n}{\lambda} sin\theta$$

and

$$(2.4) \qquad k_z = \frac{2 * \pi * n}{\lambda} cos\theta$$

where

$$(2.5) \qquad n = \frac{n_1 + n_2}{2}$$
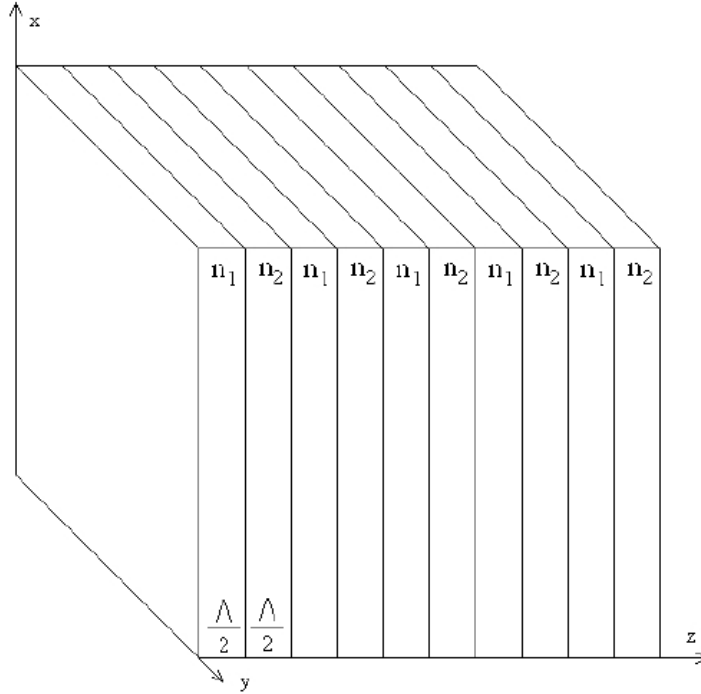
Figure 2.9: Structure of a volume Bragg grating (VBG)

In order for constructive interference (and hence high-reflectivity to occur), the phase mismatch, $\Delta\beta$ must be zero, as described in the following equation:

$$(2.6) \qquad \Delta\beta = 2k_z - m\frac{2\pi}{\Lambda} = 0$$

for odd m corresponding to the odd order Fourier components. The even Fourier components do not contribute as the coupling cancels out. First order Bragg reflection then occurs when

$$(2.7) \qquad \Lambda = \frac{\lambda}{2n * cos\theta}.$$

For most applications, the waves will be input at normal incidence, resulting in TEM propagation, so that there will be no transverse beam spreading. If, however, the incident beam is at an angle θ with respect to the grating axis, the reflection efficiencies differ by a factor of $cos(2\theta)$. Correspondingly, the efficiency of the TM wave will approach zero as θ approaches 45 degrees.

To introduce a large dispersion, the period Λ is varied linearly across the length of the grating to introduce what is primarily a quadradic phase, or linear chirp. An intuition for the operation of a chirped Bragg grating can be obtained by considering the following. Each frequency component is reflected at the axis position that satisfies the Bragg phase matching condition for that frequency, which is a linearly varying function of z. The group delay, or the time it takes for each frequency component to enter and reflect back through the grating, is thus a linear function of frequency. This results in the linear chirp than can be either positive (frequency increasing with time), typically used for stretching, or negative (frequency decreasing with time), typically used for recompressing, depending on whether the pulse enters from the longer period side (resulting positive chirp) or the shorter period side (resulting in negative chirp).

Ideally, the resulting chirp would be perfectly linear on either side so that there would be no temporal aberrations after recompression. This is not the case, however, even for a perfectly written CVBG. What is then needed for design and comparison to experiment are quantitative models that capture the full frequency response of the grating devices.

2.3.1   Coupled Mode Theory and Transfer Matrix Solution

There are multiple methods to model a chirped Bragg grating in the form of coupled mode equations and solve them via consecutive transfer matrix multiplications [43, 44, 1]. The method in [1] is particularly useful due to its simplicity and flexibility.

The physical layout is shown in Fig. 2.10, where the stack period $\Lambda = d_h + d_l$. The effective refractive index n_{eff} is then given by
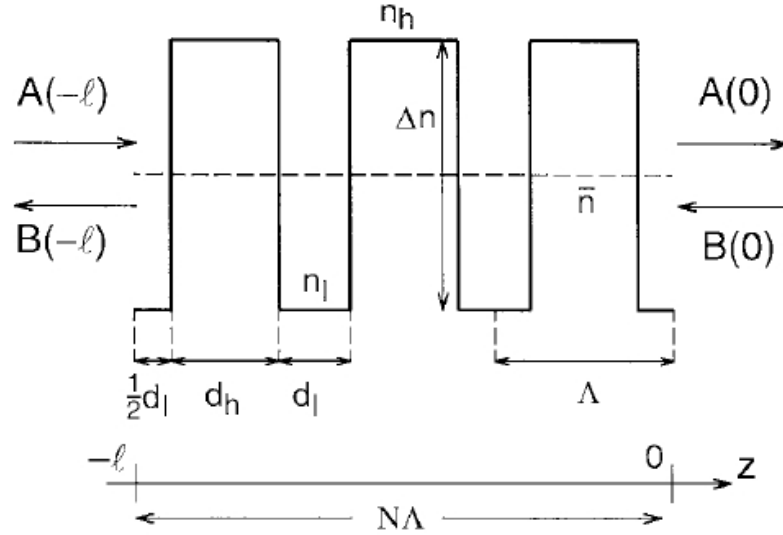
Figure 2.10: Physical model used for Transfer Matrix Method analysis [1]

$$\Lambda n_{eff} = n_h d_h + n_l d_l = d_{opt} \qquad (2.8)$$

where d_{opt} is the optical thickness of the one period of the structure. Plane wave propagation along the normal grating axis is assumed with A(z) and B(z) representing the waves traveling to the right and left, respectively. Their amplitudes are set so the energy flux in their respective direction is equal to the absolute amplitude value squared. Assuming a small Δn, the propagation of the waves are well described by the coupled mode equation system [45, 46]:

$$(2.9) \qquad \frac{d}{dz} \begin{pmatrix} A(z) \\ B(z) \end{pmatrix} = \begin{pmatrix} -i\beta & -i\kappa e^{-iKz} \\ i\kappa e^{iKz} & i\beta \end{pmatrix} \begin{pmatrix} A(z) \\ B(z) \end{pmatrix}$$

with $K = \frac{2\pi}{\Lambda}$ is the wavenumber of the dielectric stack, $\beta = k n_{eff}$ is the wavenumber in the medium, and $k = \frac{2\pi}{\lambda}$ is the wavenumber in vacuum. A coupling coefficient κ corresponds to the lowest order Fourier coefficient of the dielectric stack. Figure 2.11
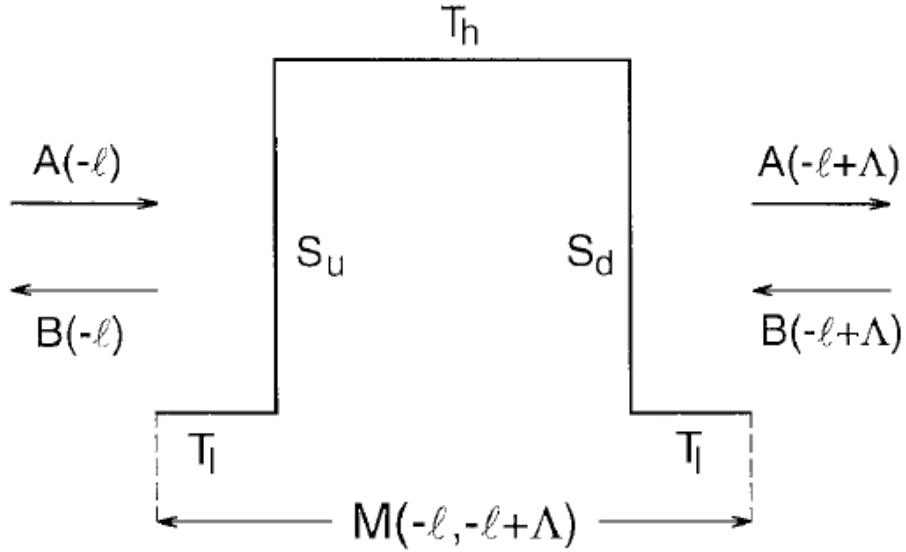
Figure 2.11: Single period in the dielectric stack chosen symmetrically for matrix computational convenience

shows a single period in the stack chosen for a symmetric profile. This makes the coupling coefficient a real negative number.

Defining $\Delta n = n_h - n_l$ and $\bar{n} = \frac{1}{2}(n_h + n_l)$, κ is evaluated:

(2.10)
$$\kappa = -\frac{2\Delta n \bar{n}}{n_{eff}} sin(\frac{K d_h}{2}) \frac{1}{\lambda} < 0$$

Evaluating the above equation at $\lambda_B = 2 n_{eff} \Lambda$, the Bragg wavelength, the coupling coefficient is simplified:

(2.11)
$$\kappa = -\frac{2\Delta n \bar{n}}{n_{eff}^2 \Lambda} sin(\frac{K d_h}{2})$$

Again, taking a small Δn, and assuming quarter-wave layers and an operating wavelength near the stop band around the Bragg wavelength, the coupling coefficient κ is further simplified to:

$$(2.12) \qquad \kappa = \frac{\Delta n}{\overline{n}\Lambda}$$

Solving the coupled mode equations between z=-l and z=0 results in the transfer matrix M(-l,0) for the Bragg grating [47]

$$(2.13) \qquad \begin{pmatrix} A(-l) \\ B(-l) \end{pmatrix} = M(-l,0) \begin{pmatrix} A(0) \\ B(0) \end{pmatrix}$$

with

(2.14)

$$M(-l,0) = (-1)^N \begin{pmatrix} cosh(\gamma\Lambda N) + i\frac{\delta}{\gamma}sinh(\gamma\Lambda N) & i\frac{\kappa}{\gamma}sinh(\gamma\Lambda N) \\ -i\frac{\kappa}{\gamma}sinh(\gamma\Lambda N) & cosh(\gamma\Lambda N) - i\frac{\delta}{\gamma}sinh(\gamma\Lambda N) \end{pmatrix}$$

given that l=ΛN is the full length of the dielectric stack of N layers. δ, the detuning coefficient that is equal to the phase mismatch between the effective wavenumber and one half of the stack's wave number is computed by

$$(2.15) \qquad \delta = \beta - \frac{K}{2} = \beta - \frac{\pi}{\Lambda}$$

and

$$(2.16) \qquad \gamma = \sqrt{\kappa^2 - \delta^2}$$

where γ is the propagation constant in the dielectric stack, which becomes imaginary outside the stop band where $\kappa < \delta$.

It is useful to compute the amplitude reflectivity of the structure, which is given by

$$(2.17) \qquad\qquad r_M = \frac{A(0)}{B(0)} = -\frac{m_{12}}{m_{11}}$$

when the right side is taken as the input side, and m_{12} and m_{11} are matrix elements of M, given above. The reflection from the left is computed in a similar fashion.

Of course, for a chirped grating, the period Λ varies over the length of the structure. To compute the transfer matrix for such a complex device, the matrix for each period must be found, and the final matrix will be computed through successive multiplications.

To find the matrix of one period, consider the single symmetric period illustrated in Fig. 2.11. The matrix of the period is given by

$$(2.18) \qquad\qquad M(-l, -l + \Lambda) = T_l S_u T_h S_d T_l$$

where T_l is the transfer matrix of half the length of the lower index layer, T_h is the transfer matrix of the full length of the high index layer, S_u is the matrix of the interface between low and high indicies, and S_d is the interface matrix for the jump from high to low index.

The propagation matrices T_h and T_l are given by

$$(2.19) \qquad\qquad T_h = \begin{pmatrix} e^{i\phi_h} & 0 \\ 0 & e^{-i\phi_h} \end{pmatrix}$$

$$(2.20) \qquad\qquad T_l = \begin{pmatrix} e^{i\phi_l/2} & 0 \\ 0 & e^{-i\phi_l/2} \end{pmatrix}$$

with $\phi_h = k n_h d_h$ and $\phi_l = k n_l d_l$. For the index discontinuities, the matrices are

$$(2.21) \qquad S_u = \frac{1}{\sqrt{n_h n_l}} \begin{pmatrix} \overline{n} & -\frac{1}{2}\Delta n \\ -\frac{1}{2}\Delta n & \overline{n} \end{pmatrix}$$

$$(2.22) \qquad S_d = \frac{1}{\sqrt{n_h n_l}} \begin{pmatrix} \overline{n} & \frac{1}{2}\Delta n \\ \frac{1}{2}\Delta n & \overline{n} \end{pmatrix}$$

with

$$(2.23) \qquad \phi = \phi_h + \phi_l,$$

$$(2.24) \qquad \Delta\phi = \phi_h - \phi_l,$$

and

$$(2.25) \qquad r = \frac{\Delta n}{2\overline{n}}.$$

Evaluating the above, the transfer matrix for one period is then

$$(2.26) \qquad M(-l, -l + \Lambda) = \begin{pmatrix} F & G^* \\ G & F^* \end{pmatrix}$$

with

$$(2.27) \qquad F = \frac{1}{1 - r^2}(e^{i\phi} - r^2 e^{-i\Delta\phi})$$

and

$$(2.28) \qquad G = \frac{-2ir}{1 - r^2}sin(\phi_h).$$

This method allows for each layer's matrix to have independent parameters from the rest of the stack. Thus, complex structures having linear or arbitary chirp (cubic, quartic and higher orders) can be modeled. And even more complex structures can be modeled, for example, those having a nonuniform Δn. This is necessary to model apodized gratings, in which the edges have lower modulation to reduce the group delay ripple. The effects of group delay ripple are covered in detail in Chapter V. Furthermore, the model can accomodate the thermo-optic effect in which the refractive index changes with temperature, and thermal-expansion effect, in which the material expands due to heat. These effects are essential for modeling the perturbations to the CVBG's dispersion at high (greater than 100 W) input laser power, which is the topic of Chapters III and IV

Due to the large number of complex matrix multiplications required to evaluate a grating, the matrix method is computationally expensive. Consider a typical CVBG with 5×10^4 layers and evaluating the transfer function for a typical 2^{13} frequency points. Approximately 4×10^8 multiplications will need to be performed. This can take several minutes or longer, even on a current computer. Though the process can be readily parallelized due to the independence of the frequency points, it is still desirable to have a faster computational model to perform a parameter sweep, even if it is not quite as flexible.

2.3.2 Analytical Chirped Bragg Grating Solution

Recently, an analytic solution for the reflection coefficient for a simple, uniform, linearly chirped Bragg grating was found [48]. Consider the scattering problem in Fig. 2.12. An electric field E(z) propagates through a dielectric stack with a weakly modulated refractive index n+δn(z) that satisfies the one-dimenstion Helmholtz equation

Figure 2.12: Physical picture of the wave interaction problem

$$(2.29) \qquad \frac{d^2E}{dz^2} + k^2[1 + 2\frac{\delta n(z)}{n} + (\frac{\delta n(z)}{n})^2]E = 0,$$

with

$$(2.30) \qquad k = \frac{\omega n}{c}$$

where z is the propagation axis, k is the vacuum wavenumber, ω is the angular frequency, and c is the speed of light. Generally, the δn term may have an amplitude and phase.

For this derivation, the index modulation is given by

$$(2.31) \qquad \frac{\delta n(z)}{n} = 2\beta cos\theta(z)$$

with β being the depth of index modulation and θ(z) is the grating phase. The quadratic term in the Helmoltz equation can be neglected for $\beta \ll 1$, which is generally true for CVBGs, which typically have $\beta = 10^{-4}$ to 10^{-3}. For a linear chirp,

$$(2.32) \qquad \theta(z) = \alpha z^2/2 + \kappa z + \theta_0,$$

where κ is the central spatial frequency, θ_0 is the phase offset, and α is the chirp rate. Slow phase variation is assumed:

$$(2.33) \qquad \left|\frac{d\theta}{dz} - \kappa\right| \ll \kappa.$$

Keeping with the notation in Fig. 2.12, let a and b represent the waves propagating in the positive (right) and negative (left) directions, respectively:

$$(2.34) \qquad E = ae^{ikz} + be^{-ikz}$$

Discarding the resonance of higher orders around deturning

$$(2.35) \qquad q = k - \kappa/2 \ll k_0 = \kappa/2$$

yields the coupled wave equations

$$(2.36) \qquad a' = ik_0\beta e^{-2ikz+i\theta(z)}b, \, b' = -ik_0\beta e^{2ikz-\theta(z)}a,$$

with the prime indicating the derivative with respect to z. Moreover, the k factor in the exponents are replaced by k_0 due to the resonance approximation [43]. Taking the derivatives with respect to z yields the second-order coupled differential equations

$$(2.37) \qquad a'' - i\alpha(z - z_0)a' - k_0^2\beta^2 a = 0,$$

and

$$(2.38) \qquad b'' + i\alpha(z - z_0)b' - k_0^2\beta^2 b = 0,$$

where z_0 is the reflection point for the central frequency given by

$$(2.39) \qquad z_0 = \frac{(2k - \kappa)}{\alpha} = 2\frac{q}{\alpha}$$

The VBG is taken to be of length 2L, so the points -L≤z≤L correspond to the grating interior. Setting the boundary condition

$$(2.40) \qquad b(L) = 0$$

provides the reflection and transmission coefficients

$$(2.41) \qquad r = \frac{b(-l)}{a(-L)},$$

$$(2.42) \qquad t = \frac{a(L)}{a(-L)}.$$

For a weak chirp, the wave equations are valid for $\alpha L \ll \kappa$.

The coupled second-order equations can be reduced to one equation:

$$(2.43) \qquad t\ddot{a} + (\frac{1}{2} - t)\dot{a} + i\eta a = 0$$

with this substitution being made

$$(2.44) \qquad t = i\alpha(z - z_0)^2/2.$$

Here the dot operators denote differentiation with respect to the variable t (not to be confused with time), and the adiabatic parameter $\eta = \beta^2 k_0^2/2\alpha$. Note that the above equation for a corresponds to the confluent hypergeometric differential equation, with known solutions. Thus, the solutions for the range $-L < z < L$ can be expressed as

$$(2.45) \qquad a(z) = A_1 u_1(z) + A_2 u_2(z), b(z) = B_1 u^*_1(z) + B_2 u^*_2(z),$$

using the Kummer confluent hypergeometric functions [49] defined by:

$$(2.46) \qquad u_1 = F(-i\eta; \frac{1}{2}; i\alpha(z - z_0)^2),$$

$$(2.47) \qquad u_2 = (z - z_0)F(\frac{1}{2} - i\eta; \frac{3}{2}; \frac{i\alpha(z - z_0)^2}{2}),$$

$$(2.48) \qquad F(a; c; x) = 1 + \frac{ax}{c1!} + \frac{a(a+1)x^2}{c(c+1)2!} + ...$$

with A_1, A_2, B_1, B_2 are constants and complex conjugation is denoted by the asterisk. Relations for the constants can be found from the coupled first-order differential equations around z_0 for a$=A_1 + A_2(z - z_0) + O((z - z_0)^2)$ and b$=B_1 + B_2(z - z_0) + O((z - z_0)^2)$:

$$(2.49) \qquad \frac{A_2}{B_1} = ik_0\beta e^{i\theta_0 - i\alpha z^2_0/2},$$

$$(2.50) \qquad \frac{B_2}{A_1} = -ik_0\beta e^{-i\theta_0 + i\alpha z^2{}_0/2},$$

and from the boundary conditions the ratio of A_1 and A_2 is given by

$$(2.51) \qquad \rho = \frac{A_1}{A_2} = \frac{B_2}{k^2{}_0\beta^2 B_1} = -\frac{F(i\eta; \frac{1}{2}; -i\alpha(L-z_0)^2/2)}{\beta^2 k^2{}_0(L-z_0)F(\frac{1}{2}+i\eta; \frac{3}{2}; -i\alpha(L-z_0)^2/2)}.$$

Finally, the transmission and, more importantly, the reflection coefficients are then obtained:

$$(2.52) \qquad t = \frac{\rho u_1(L) + u_2(L)}{\rho u_1(-L) + u_2(-L)},$$

and

$$(2.53) \qquad r = \frac{e^{i\theta_0 + i\alpha z_0^2/2}}{ik_0\beta}\frac{u_1^*(-L) + \beta^2 k_0^2 \rho u_2^*(-L)}{\rho u_1(-L) + u_2(-L)},$$

with u_1 and u_2 being defined above.

Thus, the frequency response of a CVBG can be computed analytically with negligible computational time (for example, 2^{13} frequency points can be evaluated in less than one second on a current personal computer). The caveats of this model, however, are that a purely linear chirp is assumed and the depth of index modulation is constant across the grating. Hence, the slower transfer matrix method must be used when considering more complex gratings. Nonetheless, this model is still tremendously useful for performing rapid parameter sweeps for CVBG design.

One consequence observed from both numerical methods is the presence of group delay ripple, wherein the group delay is not a simple linear function of frequency but has some modulation. Figure 5.1 plots an example of a chirped grating's group delay. This is the result from interference from the multiple dielectric layers' reflections; each layer has a finite reflectivity for all frequency components. Unfortunately, due to the non-equal wave amplitudes reaching the grating ends, the ripples do not cancel out

after the pulse is launched from each end [43], resulting in degraded recompression. Chapter V covers this effect in detail.

2.4 Chirally Coupled Core Fibers - Theory and Operation

Section 1.2 in Chapter I established the need and motivation for optical fibers that possess large-mode-areas but only allow the fundamental LP_{01} mode to progagate while suppressing all higher-order modes. Though multi-kW average [50] and multi-MW [51] peak power fiber lasers have been demonstrated with diffraction-limited performance in large-mode-area (LMA) fibers, these systems lack robustness and cannot be further scaled without increasing the core diameters even further. Chirally-coupled-core (CCC) fibers offer a solution that will allow for core scalability while maintaining robust single-mode operation for diffraction-limited output beams free of modal dispersion, essential for ultrafast CPA systems. CCC fibers can be coiled and spliced, thereby maintaining the benefits of compactness and robustness that has made fiber lasers so attractive.

Reference [2, 3] describes the basic principle of operation of CCC fibers in the scalar approximation. Figure 2.13 shows the idea behind CCC fibers. A helical side-core is wrapped around the larger main core, which carries the beam power. A simple physical concept elucidates the operation principle; since the electric fields of modes of higher order than LP_{01} tend to spread more towards the outer portion of the main core, they are preferentially coupled into the helical side-core where they can be leaked out. The challenge then for CCC fiber design is to have a high main-to-side core coupling coefficient for modes LP_{11} and higher while having a negligible coefficient for the fundamental LP_{01} mode.

Parameters for CCC fiber design include the main core diameter, side core diame-
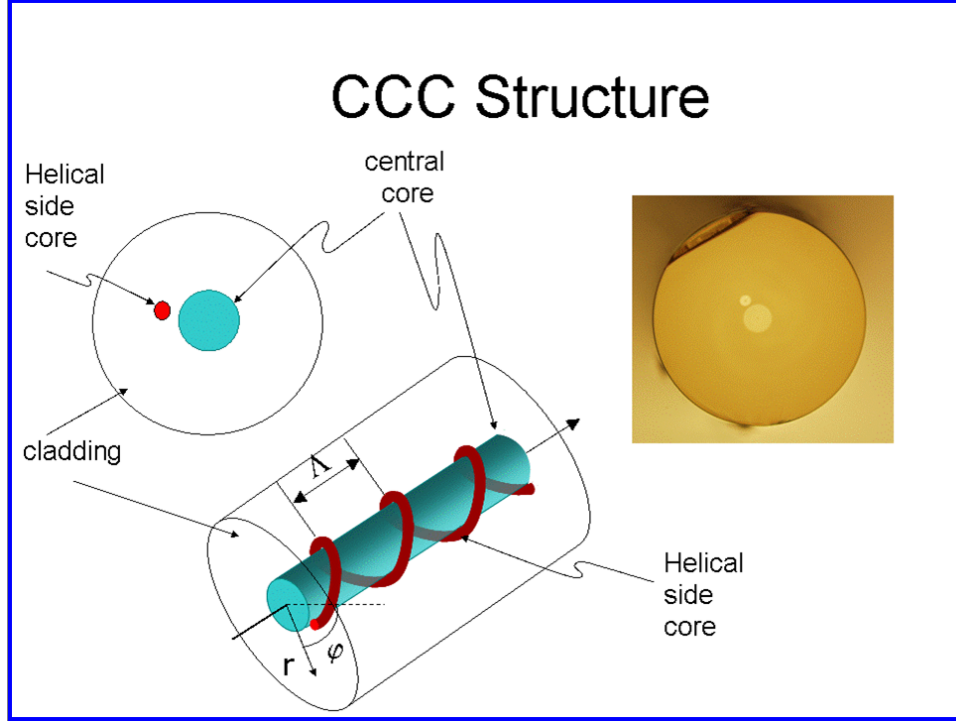
Figure 2.13: Illustration of Chirally-Coupled-Core Fibers; a helical side-core preferentially couples energy out of the higher-order modes, resulting in an effectively single-mode large-mode area fiber

ter, side core helical pitch, distance from the main-to-side cores, and refractive index difference between the cores and cladding, which determines the fiber's numerical aperture. Also, it has been found that the shape of the outer cladding, whether it is circular or rounded hexagonal, affects the pump absorption.

Analyzing the performance of the CCC fibers is done using the beam-propagation-method [2], in which the beam-propagation wave equation

$$(2.54) \qquad \frac{\partial u}{\partial x} = \frac{i}{2\overline{k}}\left(\frac{\partial^2 u}{\partial x^2} + \frac{\partial^2 u}{\partial y^2} + (k^2 - (\overline{k})^2)u\right)$$

is solved via a finite difference method.

Generally, the design goal is to maximize the core diamter while also maximizing the higher-order-mode (HOM) loss and minize the fundamental mode loss. The degree of HOM suppression required is dependent on the fiber's application. Longer fibers, such as those used for amplifiers, which are typically on the order of sev-
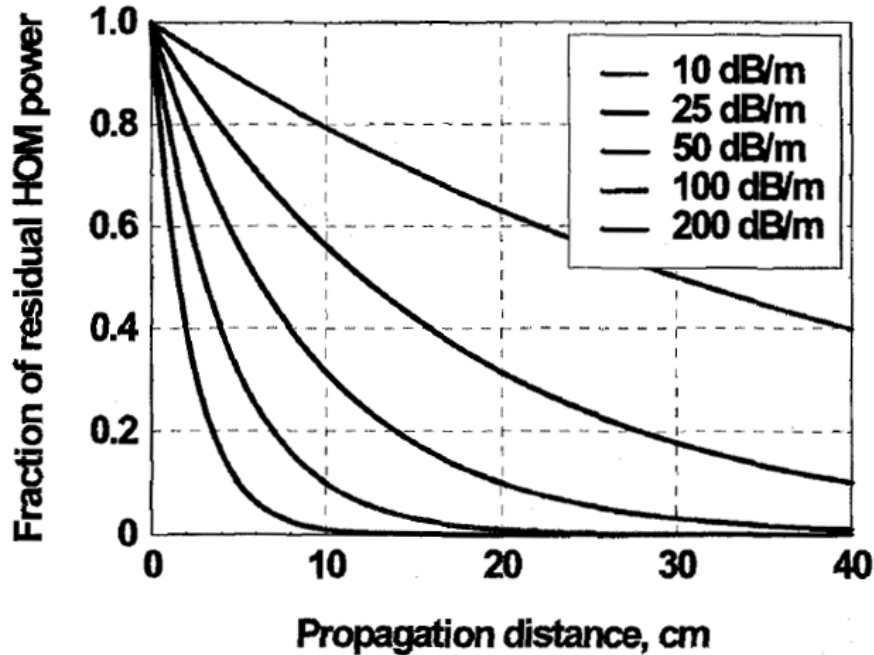
Figure 2.14: Fractional HOM residual power versus fiber length for various extinction level CCC fibers; the curves increase in HOM extention level from the top down

eral meters, need smaller suppression levels. 10 dB/m, for example, would yield 20 dB, or 99%, HOM suppression over a 2 m amplifier fiber. However, shorter fibers, such as passive pig-tail connectors for monolithic fiber components, would require substantially greater suppression as their lengths are on the order of tens of centimeters. Depending on the length and application, anywhere between 25 dB/m and 100 dB/m, or greater, would be necessary for sufficient HOM extinction. Figure 2.14 plots the residual HOM fractional power versus fiber lengths for various HOM extinction levels.

As the LP_{11} mode is the next lowest order to the fundamental LP_{01}, most design revolves around eliminating it while preserving the fundamental mode. When suitable parameters are found, the other HOMs can be checked to ensure the design is functional. A sample beam-propagation-method for the LP_{01} and LP_{11} mode losses versus the side-core helix period and numerical aperture is shown in Fig. 2.15.
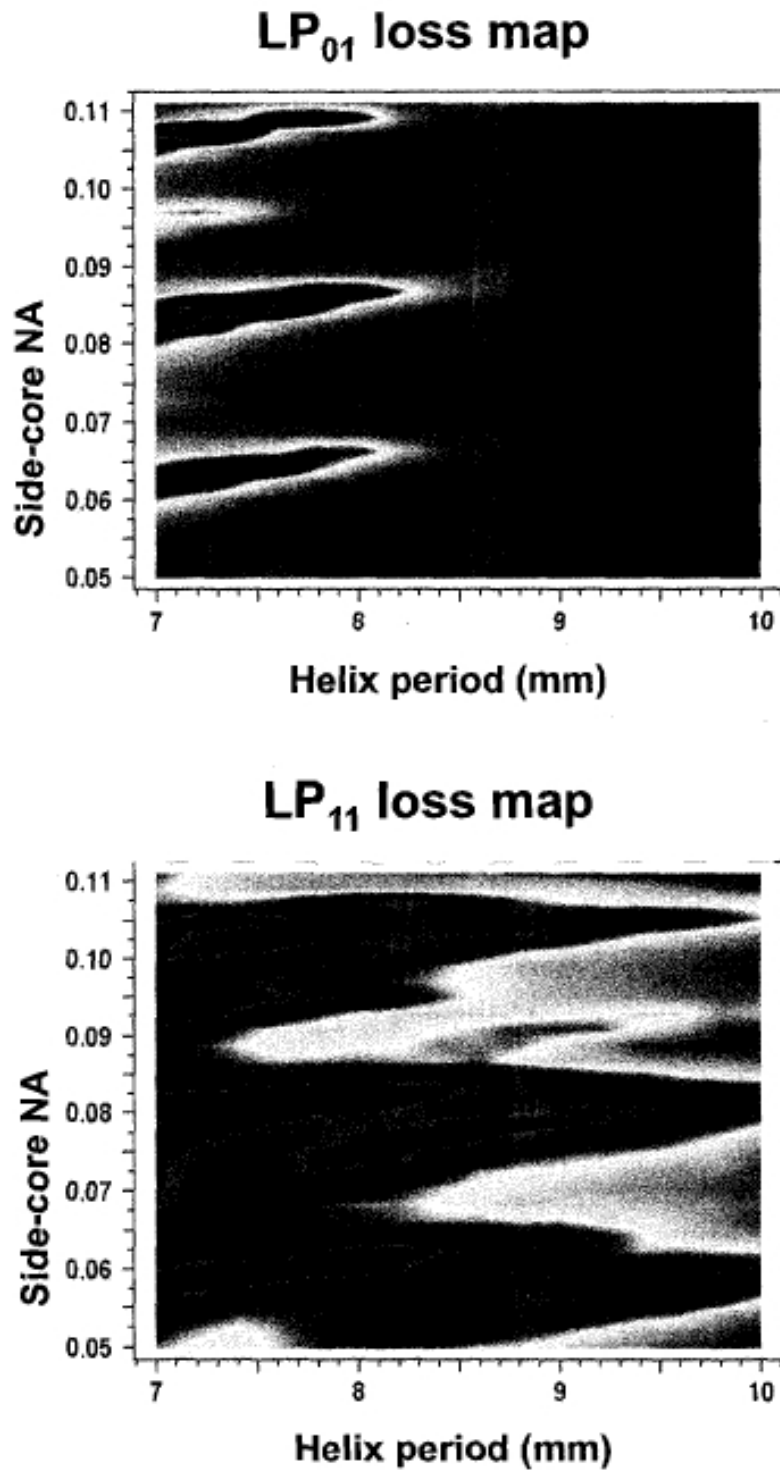
Figure 2.15: Loss in the LP$_{01}$ and LP$_{11}$ modes versus side core numerical aperature and helical pitch [2, 3]
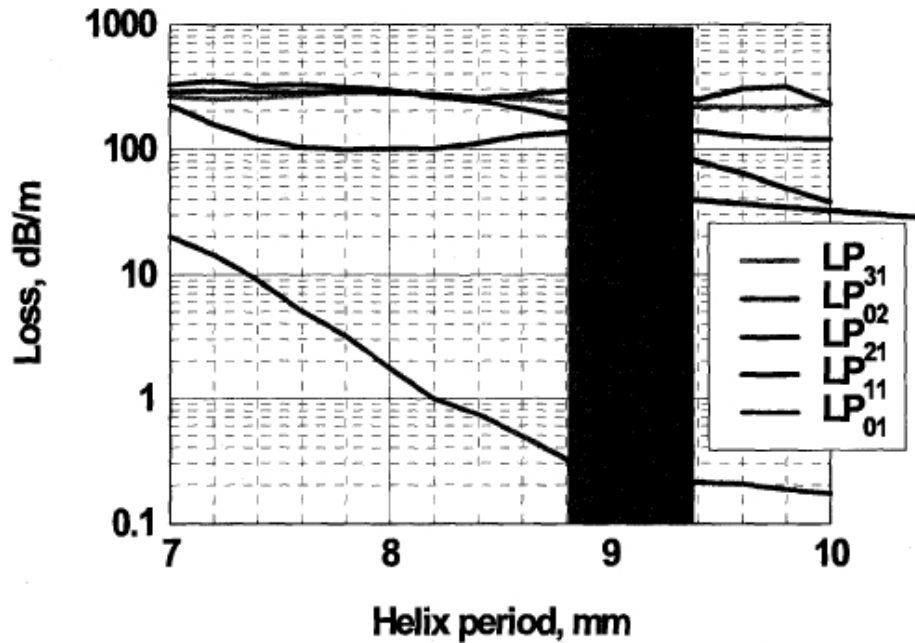
Figure 2.16: Modal loss versus side core helical pitch for a CCC fiber for several modes [2, 3]

A 1-D scan can then be performed for multiple modes for a fixed NA and varying the helix pitch, where the above figures show good HOM extinction and good fundamental mode preservation. The scan is shown in Fig. 2.16.

It can thus be seen that a helical pitch of ~ 9 mm yields excellent performance. Using this design technique, amplifier CCC fibers have been engineered and fabricated that have greater than 30 μm diameter cores with effectively single-mode operation. 1 mJ pulses at a 100 kHz repetition rate (~ 100 W average power) as well as 310 W CW operation [15, 35] have been achieved using CCC amplifier fibers. Chapter III in this thesis details a 200 W (130 W after compression) average power fiber chirped-pulse-amplification system using CCC power amplifier fibers.

It is important to note that the above review of the basic operation principles of CCC fibers structures is limited to scalar field approximation. Current ongoing complete CCC fiber theoretical decription revealed that all effects occuring in CCC

fibers require complete vectorial description of propagating fields (private communication with Xiuquan Ma), which goes beyond the scope of the short survey presented in this section.

CHAPTER III

130 W, 350 fs Fiber-CPA System based on Chirped Volume Bragg Gratings and Chirally Coupled Core Fiber Technology

130 W of power (200 W amplified) with a 350 fs pulse duration has been obtained from a fiber-CPA system based on robust chirped-volume-Bragg grating stretchers/compressors and chirally-coupled-core amplifier fibers. The efficacy of these technologies for high power operation is demonstrated.

3.1   Introduction

Ultrafast high power fiber chirped pulse amplification (CPA) lasers are promising for a wide range of applications including material processing and inspection, THz imaging, and EUV and X-ray generation. Fiber lasers are particularly attractive over conventional bulk solid-state lasers due to their potential to be made compact, since the amplifiers can be coiled, monolithic, since the components can be spliced together, and hence robust since there would be no free-space components requiring alignment. Moreover, fiber lasers can produce diffraction-limited beams even at high power due to the lack of thermal aberration. However, several challenges still need to be overcome in order for fiber CPA lasers to reach their full potential for high-average power (kW level) output femtosecond pulses while still maintaining their

compactness and robustness.

Firstly, current high-power fiber CPA systems still rely on conventional bulk grating stretchers and compressors, which are large and complex to align. This is incompatible with keeping fiber lasers compact and monolithic. A promising alternative to these systems are chirped volume Bragg gratings (CVBGs), which are slabs of glass of centimeter dimensions that can stretch and recompress ultrashort pulses with only a few nanometers of bandwidth to hundreds of picoseconds depending on their length (the chirp-rate is 100 ps/cm) [52]. This is accomplished by writing a longitudinal index of refraction profile into photo-thermo-refractive (PTR) glass in such a way that the Bragg wavelength varies linearly with position. A positive dispersion can be applied to the pulse by sending it in one way, and a reciprocal negative dispersion can be applied by sending the pulse into the opposite end of the CVBG. Due to their small size and trivial alignment, CVBGs are compatible with keeping fiber CPA lasers compact and robust. Furthermore, the excellent thermal properties of PTR glass enable CVBGs to withstand high average laser powers.

The next major challenge for fiber lasers is the development of large core area fibers that can handle high energy with minimal nonlinearity, but still provide single-mode, diffraction-limited output beams. Single-mode operation is important for lasers due to the desire to obtain the minimum spot-size for maximum intensity, and it is even more essential for ultrafast lasers since modal dispersion will result in temporally broadened pulses. Conventional large-mode-area fibers (tens of μm in diameter) can withstand high energies, however, as the core size increases, robust single-mode operation becomes nearly impossible. There are several proposed technologies to overcome this limitation including PCF rods [26], leakage-channel fibers [31], and forced higher-order mode operation of LMA fibers [53]. These have the disadvantages

of limited robustness and compactness (the PCF rods cannot be coiled) as well as the lack of ability to be spliced. The most promising new technology however is chirally-coupled-core (CCC) fibers, which are essentially LMA fibers that have a smaller helical core wrapped around the main core, which preferentially couples higher-order modes out. The result is an effectively single-mode fiber with a large mode area. Some major advantages CCC fibers have over PCF rods is that they can be bent, making it possible to keep the amplifiers compact, and they can be spliced, allowing for monolithic architectures.

In this work an Yb-fiber-CPA system based on a CVBG stretcher and compressor as well as CCC fiber amplifiers is demonstrated. 200 W of power is achieved (130 W compressed) with pulse durations of 350 fs. This is made possible by a newly fabricated CVBG that has a bandwidth of 27 nm, and in contrast to previous works [54, 55], is spatial chirp free over the entire spectral window. The efficiency of the CVBG is shown to be independent of the input power, and the beam quality is shown to be good even at high power. A thermal analysis of the CVBGs suggests that kW-class systems should be achievable with this technology.

3.2   Experimental Setup

The experimental setup is shown in Fig. 3.1. The system is seeded with a Nd:Glass oscillator generating 110 fs pulses at a repetition rate of 72 MHz with a central wavelength of 1064 nm. A negative dispersion device is used to cancel out the residual fiber dispersion, since the stretcher and compressor are intrinsically reciprocal. In this experiment, a miniature 2-grating Treacy compressor is used. However, this is merely for experimental convenience. In a production system, an appropriate length of anomalous dispersion fiber, such as properly engineered photonic band-gap fiber,
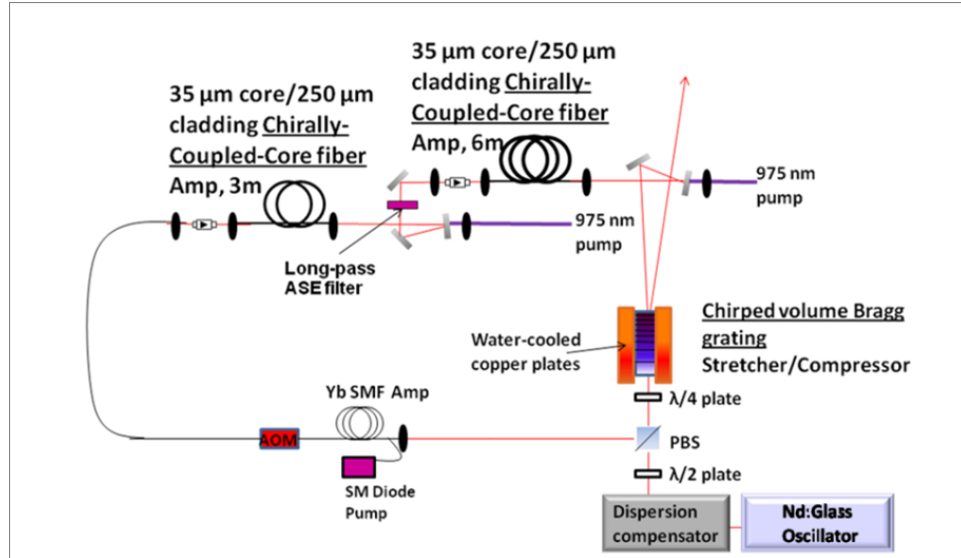
Figure 3.1: Experimental setup of high-power CVBG/CCC based fiber-CPA laser.

would be used in order to prevent using free-space components. The pulses are then sent into the broadband, 3 cm long CVBG stretcher, after which they have an edge-to-edge pulse duration of 300 ps.

A chain of three amplifiers is used to increase the power to as high as 200 W. All three amplifiers are diode-pumped at 975nm and operate in a counter-propagating configuration. The first amplifier is a standard single-mode Yb-doped fiber, used primarily to compensate for the losses due to the stretcher and dispersion compensator. Following that is a 3 m long, 35 μm diameter core/250 μm diameter cladding chirally-coupled core amplifier fiber that brings the power to 2 W. A long-pass filter to block the ASE is placed after the amplifier since not all of the pump power is extracted in this stage. The final amplifier is a 6 m long CCC fiber amplifier with the same design specifications as the previous stage, which boosts the power to its final level. The CCC amplifier fibers are robustly single-mode and require simple alignment to maximize the power throughput.

For compression, the same CVBG that is used for the stretcher is used to ensure
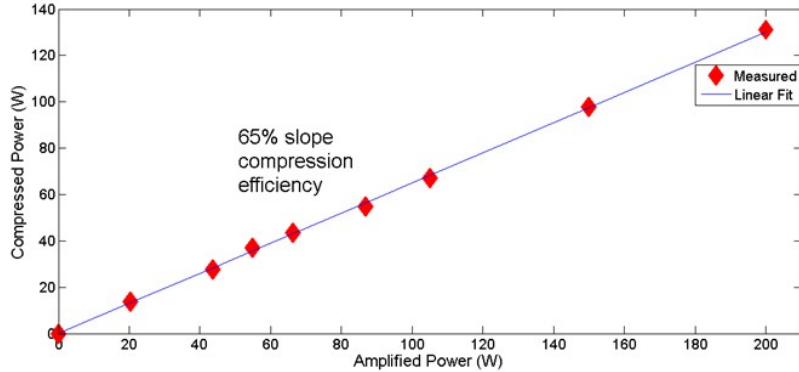
Figure 3.2: Measured compressed power vs. amplifier output for the CVBG compressor with a linear fit

accurate reciprocity. The beam is sent in at a small angle (approximately one degree) to prevent crosstalk and to avoid the need for any isolators or other transmission components that could burn at high power. Though the compressed beam is at a small angle, it roughly overlaps the stretched beam so that they will experience the same thermal load. A pair of water-cooled copper plate mounts further reduces the thermal effects on recompression, which will be shown to be necessary to preserve temporal fidelity.

3.3 Results and Analysis

An essential property that a CVBG compressor must have for high-power compatibility is an independence of diffraction efficiency on input power. Figure 3.2 shows the measured compressed power as a function of the amplifier output. The agreement with the linear fit indicates that the compressor has a 65% efficiency that is indeed independent of the input.

Furthermore, it is essential that the output beam quality not degrade as the power is increased. The beam profiles of the direct CCC fiber output, as well as the compressed beam profiles at 5 W (b), 50 W (c), and 105 W (d) of incident power
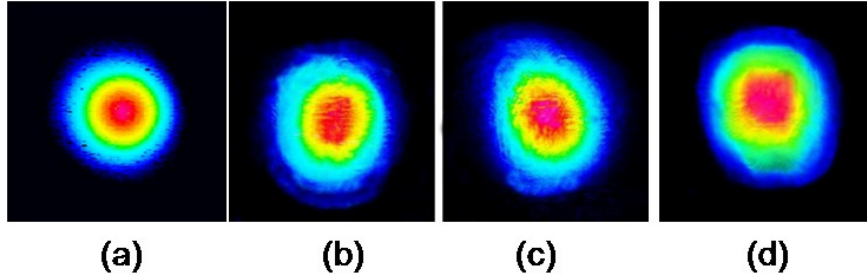
Figure 3.3: Beam profiles: (a) CCC amp. output; (b) compressed beam with 5W onto CVBG, (c) 50W onto CVBG and (d) 105W onto CVBG

onto the grating, are shown in Fig. 3.3. The lack of change in the profiles indicates that the CVBGs do not suffer from transverse thermal distortions and are again compatible with high-power operation. Moreover, the profiles shown confirm that, indeed, the CVBGs are spatial-chirp-free.

The autocorrelation measured at high power is shown in Fig. 3.4, with the corresponding compressed spectrum in the inset. For comparison, the theoretical transform-limited autocorrelation, computed from the Fourier transform of the spectrum, is also plotted. At 150 W of amplified power, the deconvolved FWHM pulse duration is 320 fs, and at 200 W, it is 350 fs. This is a record for this power level for a CVBG-based FCPA system.

Figure 3.4 also shows the computed effects due to self-phase modulation in the amplifiers as well as the perturbation of the compressor dispersion due to the thermal load based on a 3D finite-element analysis. In this model, the temperature distribution is computed inside the CVBG taking into account the spatial-spectral beam distribution in the grating based on the Bragg condition and also taking into account the boundary conditions from the cooled copper plate interfaces. Thus given the input spectrum, power, and grating absorption coefficient (10^{-2} cm^{-1} exponential absorption in this work), the temperature can be computed 3-dimensionally in the CVBG, and hence the change in index of refraction due to the thermo-optic effect
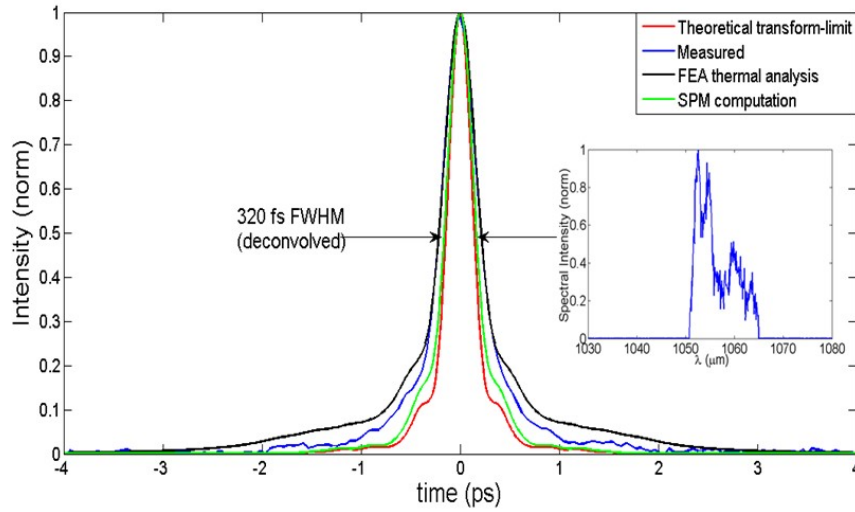
Figure 3.4: Measured autocorrelation at high-power and comparison to the theoretical transform limit, and effects due to thermal load and nonlinearity. Inset: Corresponding high-power spectrum

(with the thermo-optic coefficient being equal to that of BK7) will be known. The perturbation to the dispersion can easily be calculated by standard transfer matrix techniques, and hence the final pulse can be modeled given the input spectrum.

It is shown that there is only marginal broadening due to SPM, taking into account that the quadratic phase can be compensated for by the variable dispersion device after the oscillator. The thermal analysis indicates that the measured deviation from the transform-limit is primarily due to the load on the compressor. Recent improvements in PTR glass fabrication decrease the absorption coefficient from 10^{-2} cm^{-1} in the grating used in this work to less than 10^{-3} cm^{-1}, which will make this thermal contribution negligible.

3.4   Conclusion

Chirped volume Bragg gratings and chirally-coupled-core fiber technology have enabled the development of a fiber-CPA system that can generate 200 W of output power (130 W compressed) with pulse durations of 350 fs. CVBGs are shown to be

able to handle very high average powers, and yet are simple and compact, making them compatible with the benefits of fiber lasers. Refinements in manufacturing technique have eliminated spatial-chirp in the gratings. Chirally-coupled-core fibers provide large mode areas with robust single-mode operation. With their ability to be coiled and spliced, they are ideal candidates for next-generation monolithic systems. The data and analysis has shown the potential for further power scaling (kW level) while still maintaining few hundred femtosecond pulses. Work towards a kW-class FCPA system with these technologies is in progress.

CHAPTER IV

Analysis of Thermal Loading Effects on Chirped Volume Bragg Grating Dispersion

A model is developed to compute the dispersion of chirped-volume-Bragg-grating stretchers and compressors under sufficiently high-power conditions to generate a non-uniform thermal distribution. Agreement with experimental results is demonstrated. The ramifications of the dispersion perturbations are analyzed, and the potential for kW-level power scaling is established.

4.1   Introduction

Chirped-volume-Bragg-gratings (CVBGs) are compact and robust devices that can be used to stretch and compress pulses for chirped-pulse-amplification (CPA) lasers and offer tremendous benefits over their bulk diffraction grating alternatives. First and foremost, they are small; with only a few centimeters of length, a CVBG can stretch a transform-limited femtosecond or few-picosecond pulse to hundreds of picoseconds (the chirp rate is 100 ps/cm-length) and recompress back. This greatly reduces the footprint of a CPA system, and is essential for preserving the advantages of a fiber-laser system. Moreover, their operation is trivial; all that must be done is to send a pulse into one end of the grating, and a stretched or recompressed (positive or reciprocal negative dispersion depending on orientation) pulse will be reflected

back. This makes them ideal for monolithic systems in which free-space components with complex alignment are unusable. Furthermore, these devices are polarization independent, and have been shown to have excellent power and energy handling capabilities [56, 20] due to their being made of photo-thermo-refractive (PTR) glass.

Recently, recompression down to 350 fs was achieved at 200 W of input power from an Yb-fiber-CPA laser using a 25 nm bandwidth CVBG for the stretcher and compressor [56]. A natural question arises as to how much power can be tolerated before the CVBG dispersion properties are substantially degraded due to the thermo-optic effect or thermal expansion. Indeed, in [56], the recompressed pulses deviated from the transform-limit due to the thermal load. Clearly, this effect needs to be quantified in order to properly engineer a high-power system and so the device limits will be known.

In this work, a numerical model, based on finite-element-analysis (FEA) for the thermal effects and transfer matrices for the dispersion of CVBGs, is developed that possesses the flexibility to allow for arbitrary grating parameters and beam overlapping. The thermal effects are analyzed for a variety of likely scenarios. Experimental results are used to benchmark the model. And finally, the necessary conditions for high temporal-fidelity kW-level operation are computed.

4.2 Thermal model

Several steps are required to compute the power-dependent dispersion of CVBGs. First, the longitudinal power distribution must be known. This is computed analytically. With the knowledge of the power distribution along with the gratings absorption coefficient (the absorption is taken to be exponential) and the boundary conditions (i.e. the gratings may be cooled, which can be approximated by holding

the sides at fixed temperature, or there may be convection or insulation conditions), the temperature may be computed at all points in 3D space using FEA techniques. The temperature distribution is easily converted to index of refraction perturbations via the thermo-optic coefficient, which is approximately that of BK7 glass. Transfer matrices are then used to compute the resulting grating dispersion. This section described each of these steps in detail.

In order to compute the longitudinal power distribution, it is first observed that the optical power gradient present in the CVBGs is caused not by the material absorption, which is 10^{-2} cm^{-1} or less for the current generation of gratings, but rather by the gratings spectral reflection characteristics, i.e. the local Bragg condition will cause the power to spread depending on the spectrum. This effect can be computed analytically. Equation 4.1 provides an expression for the power distribution for a given spectrum.

$$(4.1) \quad P(z)_0 = R \int_{\Lambda_b}^{\lambda_{max}} (e^{-\alpha * z_0} S_\lambda + e^{-\alpha(2z_{refl} - z_0)} S_\lambda) d\lambda + (1 - R) \int_{-\infty}^{\infty} e^{-\alpha * z_0} S_\lambda d\lambda$$

with

$$(4.2) \qquad \Lambda_b = \lambda_{min} + \frac{\lambda_{max} - \lambda_{min}}{L} z_0$$

and

$$(4.3) \qquad z_{refl} = \frac{\lambda - \lambda_{min}}{\lambda_{max} - \lambda_{min}} L$$

Here, S_λ is the input pulse spectrum (which yields the total power when integrated over λ), α is the material absorption, R is the grating reflectivity, L is the
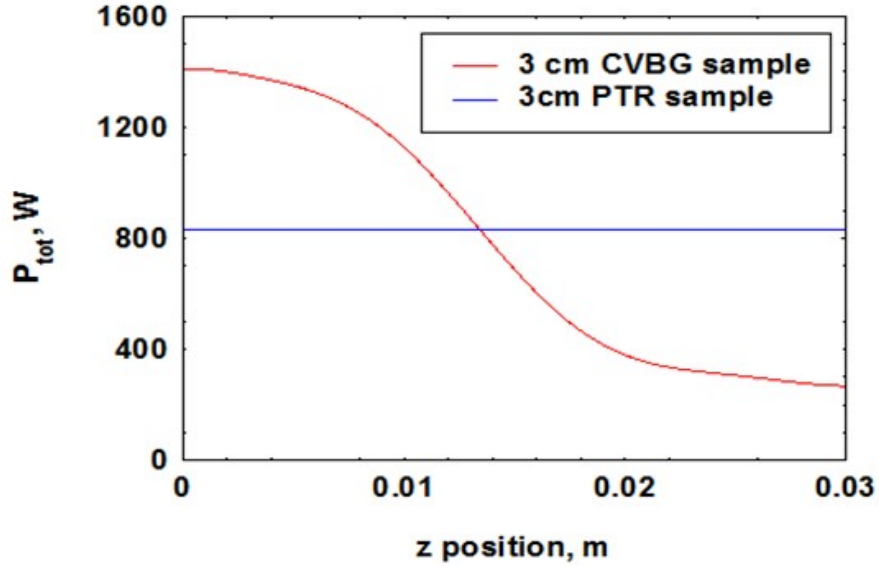
Figure 4.1: Comparison of optical power distribution along CVBG and PTR glass samples for 830 W of incident power

grating length, λ_{min} is the shortest wavelength in the reflection window and λ_{max} is the longest wavelength. For comparison, and to show that the longitudinal power distribution is indeed cause by the grating effect and not by absorption, Fig. 4.1 shows a sample calculation for both the above equation and the power distribution due only to exponential absorption in a blank slab of PTR glass (with 0.01 cm^{-1} absorption). As can be seen, the grating effect is dominant.

Given the longitudinal power distribution, the 3D temperature in the CVBG can be computed using finite-element analysis (FEA) to solve the heat transfer equation:

(4.4)
$$\nabla(-k\nabla T) = Q$$

where k is the thermal conductivity (generally a tensor, but is a scalar for thermally isotropic materials such as photo-thermo refractive glass), T is the temperature, and Q is a heat source (or sink, depending on the sign) in units of power/volume.

The program used for the calculations in this work is COMSOL Multiphysics.
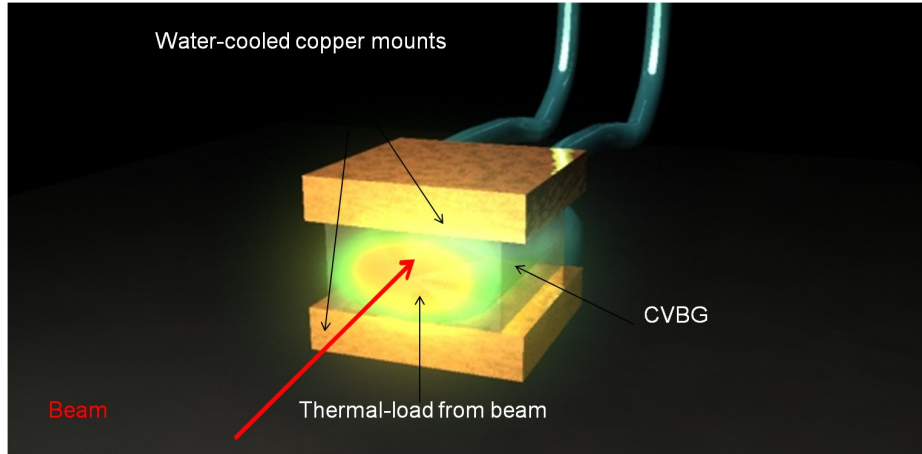
Figure 4.2: Model setup: A CVBG is sandwiched between two water-cooled copper plates while the incoming beam produces heat

Using numerical methods allows for generalizing the model to include cooling (e.g. water-cooled copper plates) as well as spatial overlapping of the stretched and compressed beams (so they encounter the same thermal distortion) in the gratings, whether complete, partial, or not at all due to angle and displacement. This makes it possible to accurately simulate the experimental conditions. Figure 4.2 illustrates the setup that is modeled.

The boundary conditions are set according to the cooling system, with both the top and bottom of the CVBGs placed in direct contact with water-cooled copper mounts. This is well approximated by setting these surfaces to a constant temperature (15 K below ambient in this work). The remaining surfaces are taken to be insulated. Though convection cooling from the air can be taken into account, it is found to be negligible and therefore needlessly increases computation time. The heat source Q in Eq. 4.4 is obtained by multiplying the power at position z from Eq. 4.1 by the absorption coefficient and distributing the power over the beam area (all beams in this work are taken to be Gaussian). Figure 4.3 shows a sample COMSOL output screen of the 3D CVBG surface temperature, and Fig. 4.4 shows a
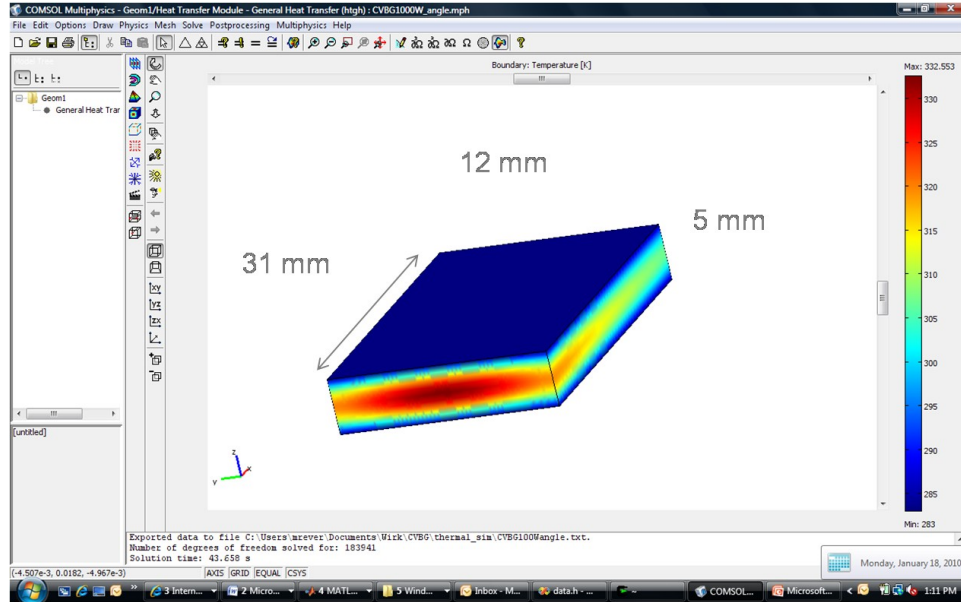
Figure 4.3: CVBG 3D surface temperature computed with COMSOL Multiphysics software
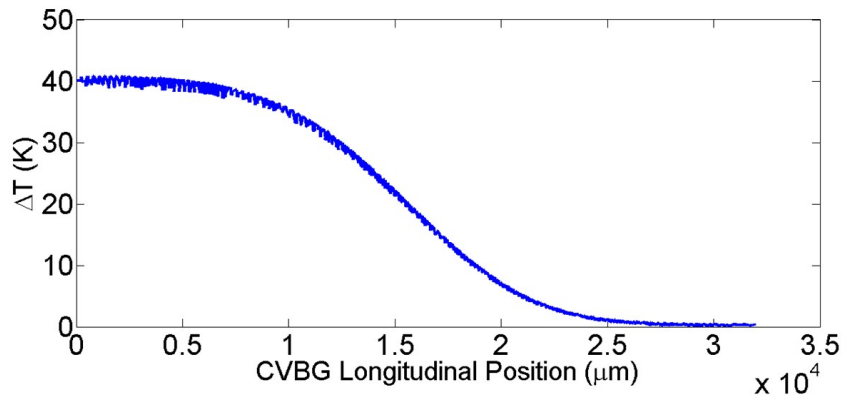
Figure 4.4: Positional temperature differential from FEA computation

sample longitudinal temperature dependence calculation from the model, for a 25 nm bandwidth CVBG centered at 1064 nm that is 3.2 cm long with 200 W of input power.

Once the temperature is known, the frequency response function of the CVBG can be computed via the matrix method presented in [44], with the thermal effects included by modifying the index of refraction in proportion to the thermo-optic coefficient and the width according to thermal expansion. The resulting cross-coefficients

in the matrix yield the CVBG frequency transfer function.

The transfer function can be computed with or without thermal perturbations, at arbitrary beam positions on the CVBG face, and for varying input angles (provided the angles are reasonably small). This allows for computation of the recompressed pulses for a wide variety of experimental conditions.

4.3   Numerical results

The common CVBG parameters used in this work are as follows. To facilitate comparison to experiment, the transverse dimensions are 5 mm by 12 mm (with a beam $1/e^2$ diameter of 3 mm). The thermo-optic coefficient is 8.6×10^{-6} K^{-1} and the thermal expansion coefficient is 0.55×10^{-6} K^{-1}. The remaining material parameters are taken to be the same as silica glass (a stock material defined in COMSOL), which is consistent with PTR glass properties [57]. The input spectrum is taken to be Gaussian with a central wavelength of 1064 nm with an 8 nm FWHM.

It is important to note that, in experiment, perfect beam overlapping between the stretched and compressed beams generally cannot be used due to crosstalk. Therefore, the compressed beam is sent into the CVBG at a small angle (3 degrees) so it can be safely dumped on the other side. Ideally, the beams would be perfectly overlapped so as to obtain reciprocal stretcher and compressor thermally distorted dispersion. Figure 4.5 (green curve) illustrates the effect that the non-ideal overlapping has on the recompressed pulses for an 80% efficient, 3 cm long, 10 nm bandwidth CVBG for 100 W of input power with an absorption of 0.01 cm^{-1}.

Figure 4.5 shows the recompressed pulse autocorrelations as a function of input power, and Fig. 4.6 shows the FWHM duration power dependence. As can be seen, the thermal effects have a much more profound effect on the wings than on the main
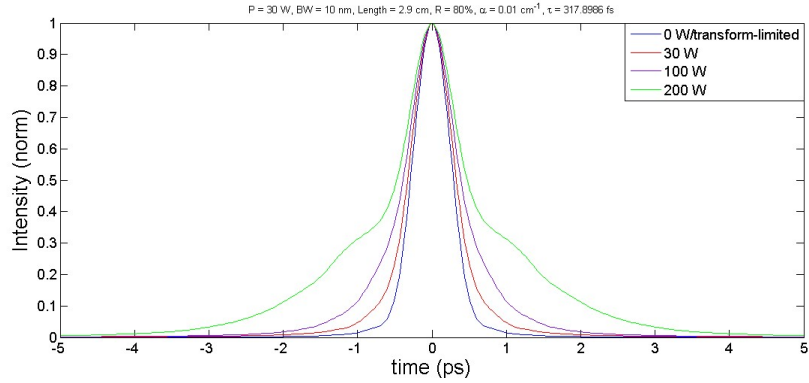
Figure 4.5: Computed recompressed autocorrelations for various input powers
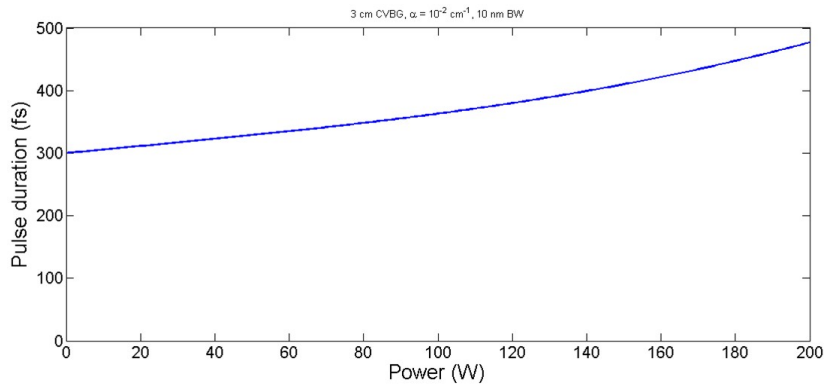
Figure 4.6: Recompressed pulse duration vs. input power for 10 nm CVBG

pulse peak.

It is necessary to know how various grating parameters, i.e. length, bandwidth, and efficiency effect the power handling capacity. Figure 4.7 shows the resulting recompressed pulses for various parameters. Also, it is important whether the choice of CVBG orientation, i.e. positive stretcher/negative compressor dispersion or vice versa affects the compressibility. Figure 4.8 demonstrates the lack of dependence on the orientation.

4.4   Comparison to experiment

To verify the efficacy of the model, the autocorrelations computed at various powers and overlap conditions are compared to measurements. Reference [56] details
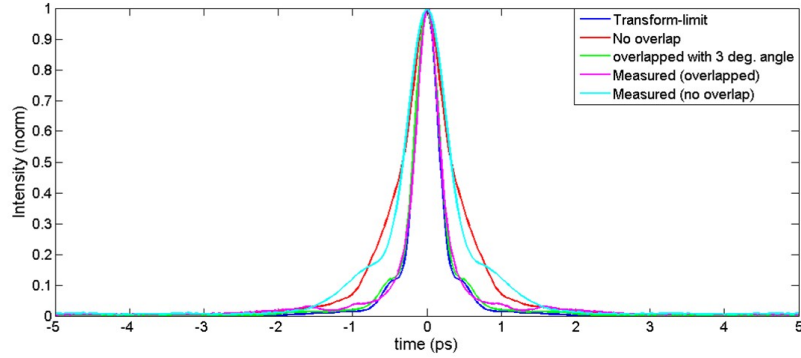
Figure 4.7: 50 W autocorrelations, theoretical and measured

the experimental setup, in which a 27 nm, spatial-chirp-free CVBG centered at 1064 nm is used to recompress a 200 W input beam (72 MHz repetition rate) from an Yb-fiber CPA laser down to 350 fs pulses.

At low power ($<$ 10 W), the resulting pulses are found to be transform-limited (computed from the zero-phase FFT of the measured compressed spectrum) both in theory and measurement. At a moderate power of 50 W, a deviation from the transform-limit is observed, as shown in Fig. 4.7.

The plot shows good agreement between the model and the experiment. Also, the data shows that overlapping the beams is essential in obtaining high-fidelity recompressed pulses. Note that the optimal case of perfectly overlapping the beams results in transform-limited pulses, however, to avoid crosstalk and damage to the system, the compressed beam must be at a small angle with respect to the grating (and the stretched beam). Hence there will always be some temporal distortion that is in proportion to the incident laser power but inversely proportional to the CVBG absorption coefficient.

Good agreement between the analysis and the measured data is also seen at higher powers, shown in Figures 4.8 and 4.9, corresponding to 100 W of incident power and 150 W of incident power, respectively.
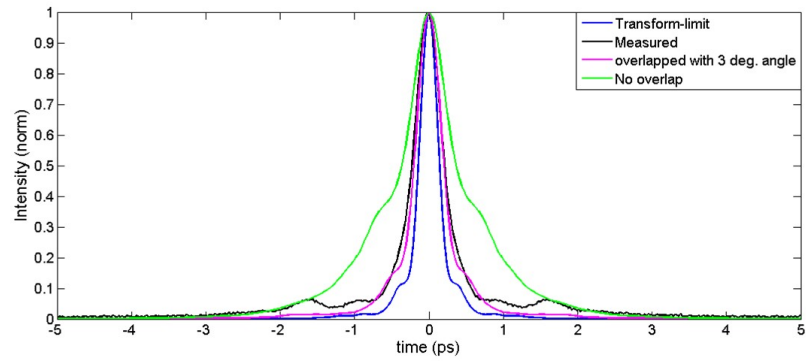
Figure 4.8: 100 W autocorrelations, theoretical and measured
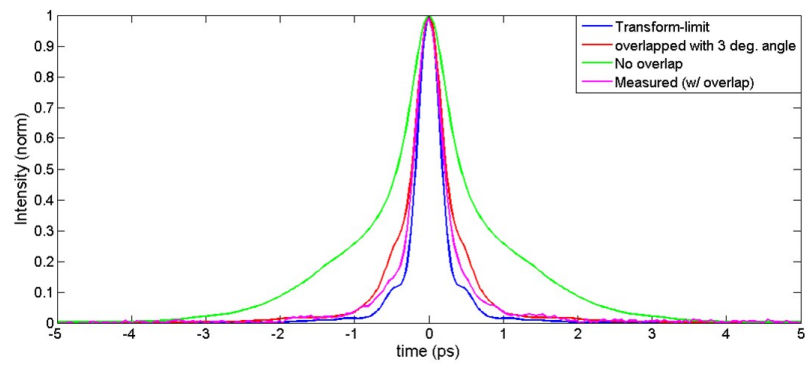
Figure 4.9: 150 W autocorrelations, theoretical and measured
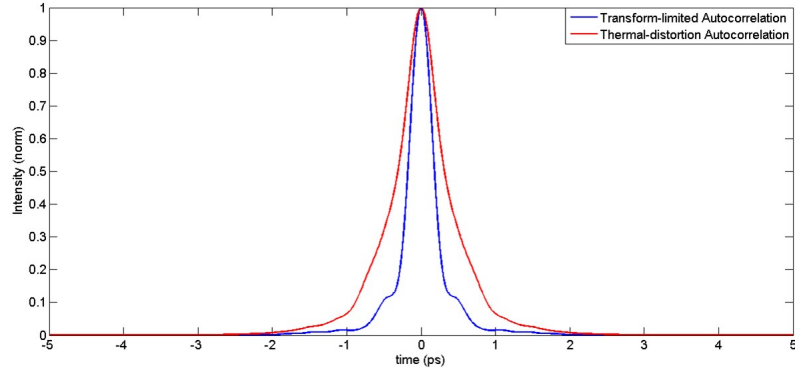
Figure 4.10: 1 kW autocorrelation w/ 10^{-3} cm^{-1} absorption and partial stretched/compressed beam overlap (3 degrees compressor angle, 1 stretched/compressed beam mm offset)

These plots indicate that the 3D model captures the power effects on the grating dispersion. Therefore, the performance at higher powers can be extrapolated.

4.5 kW-level scaling

Given that the model agrees well with the experimental data, predictions can be made by extrapolating the model to higher powers. Significant distortions to the dispersion can already be seen at 150 W of input power. Therefore, a lower absorption CVBG is needed. Recent advances in manufacturing technique have allowed for the production of a CVBG of identical characteristics as the one used in the previous experiment, but with an absorption of $< 10^{-3}$ cm^{-1}. Figure 4.10 shows the resulting computed recompressed autocorrelation at 1 kW of input power with the given grating parameters with a 3 degree angle of incidence for the compressed beam, normal incidence for the stretched beam, and a 1 mm lateral offset.

This indicates that CVBGs will be able to yield few hundred femtosecond pulses at even the kW level with a properly designed system.

4.6 Conclusion

Thermal loading is shown to have a significant effect on CVBG dispersion at significant input power levels (tens of Watts and greater). A numerical model based on FEA methods for the temperature distribution and transfer matrices for the dispersion has been developed that accurately captures this effect based on comparison to experiment. From the analysis, it is concluded that thermal control (via cooling) is needed, and the stretched and compressed beams should be overlapped as much as the experiment will allow so the thermal distortions will cancel out. Extrapolation to higher powers indicates that, given CVBGs with $\alpha \leq 10^{-3}$ cm^{-1} absorption, kW operation with few hundred femtosecond operation will be possible.

CHAPTER V

Temporal Reciprocity of Chirped Volume Bragg Grating Pulse Stretchers and Compressors

5.1 Introduction

Chirped-volume-Bragg-grating (CVBG) stretchers and compressors are practical alternatives to their conventional bulk diffraction-grating counterparts due to their compact, centimeter-scale size and robust, straightforward operation. A well known fact from dispersion compensating fiber-Bragg gratings is that, due to the interference from the refractive index discontinuities at the edges, the induced temporal phase has non-periodic oscillations resulting in group-delay ripple (GDR) that does not cancel after the pulse is sent into the opposite side [43]. The non-reciprocal GDR can result in recompressed pulses that broaden from their transform-limits as well as suffer from degraded pre-pulse contrast [58].

Clearly, the temporal degradation as a function of controllable chirped-Bragg-grating parameters, namely length, bandwidth, and depth-of-index-modulation, needs to be quantitatively characterized to determine the fundamental performance limitations. Section 5.2 surveys the existing numerical models for computing chirped-Bragg-grating frequency transfer functions. Using these models, the magnitude of the GDR is obtained and the effects on the recompressed pulse durations and contrast are examined, as shown in Section 5.3. To benchmark the models and to evaluate the

65

efficacy of CVBGs for CPA systems, Section 6.2 presents the measured recompressed pulse autocorrelations of actual CVBGs of varying bandwidths which are then compared to theory. Included are two extreme cases of highly reciprocal and highly non-reciprocal responses. Finally, the effects of GDR reduction via the technique of tapering the refractive index near the grating ends, commonly known as apodization, are investigated and show substantial amelioration for the non-reciprocal CVBGs.

5.2 Chirped Bragg Grating Models

Modeling of chirped Bragg gratings can be done using the Transfer-Matrix-Method (TMM) [43, 1] or by direct integration of the coupled-mode equations. The TMM is most widely used due to its versatility; the parameters for each layer in the dielectric stack, such as width and index-of-refraction, can be chosen independently of the other layers. This allows for the modeling of non-uniform CBGs such as those that have been apodized (to reduce the ripple, discussed in Section 5) [43] or CBGs with deleterious characteristics such as inhomogeneous writing or thermal effects [57]. However, this method is somewhat computationally expensive as it requires thousands to tens of thousands of complex matrix multiplications (one matrix per layer) to be computed for each frequency point.

The frequency transfer function of a chirped Bragg grating can be computed analytically if a simple quadratic-phase (linear chirp) is assumed across a uniformly-modulated grating as shown in [48]. By casting the grating response in the form of Kummers confluent hypergeometric functions, the reflectivity and phase responses can be obtained with negligible computational time. The model provided in [48] is the most efficient for exploring the effects on reflectivity and group delay ripple for the given grating parameters, i.e. length, bandwidth, and depth of index modulation,

but lacks the generality to capture the effects of a varying index profile, such as that of an apodized grating.

In this work, the analytic formulas are used to establish in what parameter regimes CVBGs can be used without concern for imperfect temporal reciprocity. For the cases where the group-delay ripple is severe to the extent of causing substantially degraded recompression, apodization is considered and therefore the TMM must be used.

5.3 Theoretical Results

As observed in [48], a larger chirp parameter (bandwidth per grating length) results in reduced group-delay ripple and hence better temporal fidelity. This means that, for a fixed length, reciprocity is enhanced with increasing bandwidth. CVBGs in the current generation have reflectivities of ~80% (higher for narrow-band, sub-nm bandwidth gratings) and lengths of approximately 3 cm, and it should be noted that in the context of chirped-pulse amplification, long length is desired so as to obtain greater stretched pulse durations for nonlinear phase reduction. Hence, the first important question to answer is how does the GDR magnitude depend on the bandwidth and consequently by how much will the recompressed pulses deviate from their transform-limits.

Figure 5.1 shows some sample frequency responses for 3 cm long, 80% efficient CVBGs for varying bandwidths. As can be seen, the group delay ripple becomes quite small (a few ps) for bandwidths above 2 nm. Figure 5.2 shows the recompressed pulses for the various bandwidths, assuming a square-spectrum input that fills the grating window, and Fig. 5.3 contains a plot of the FWHM recompressed pulse durations as well as the corresponding transform-limited durations (i.e. pulses that contain the reflectivity ripple but not the residual group delay ripple).
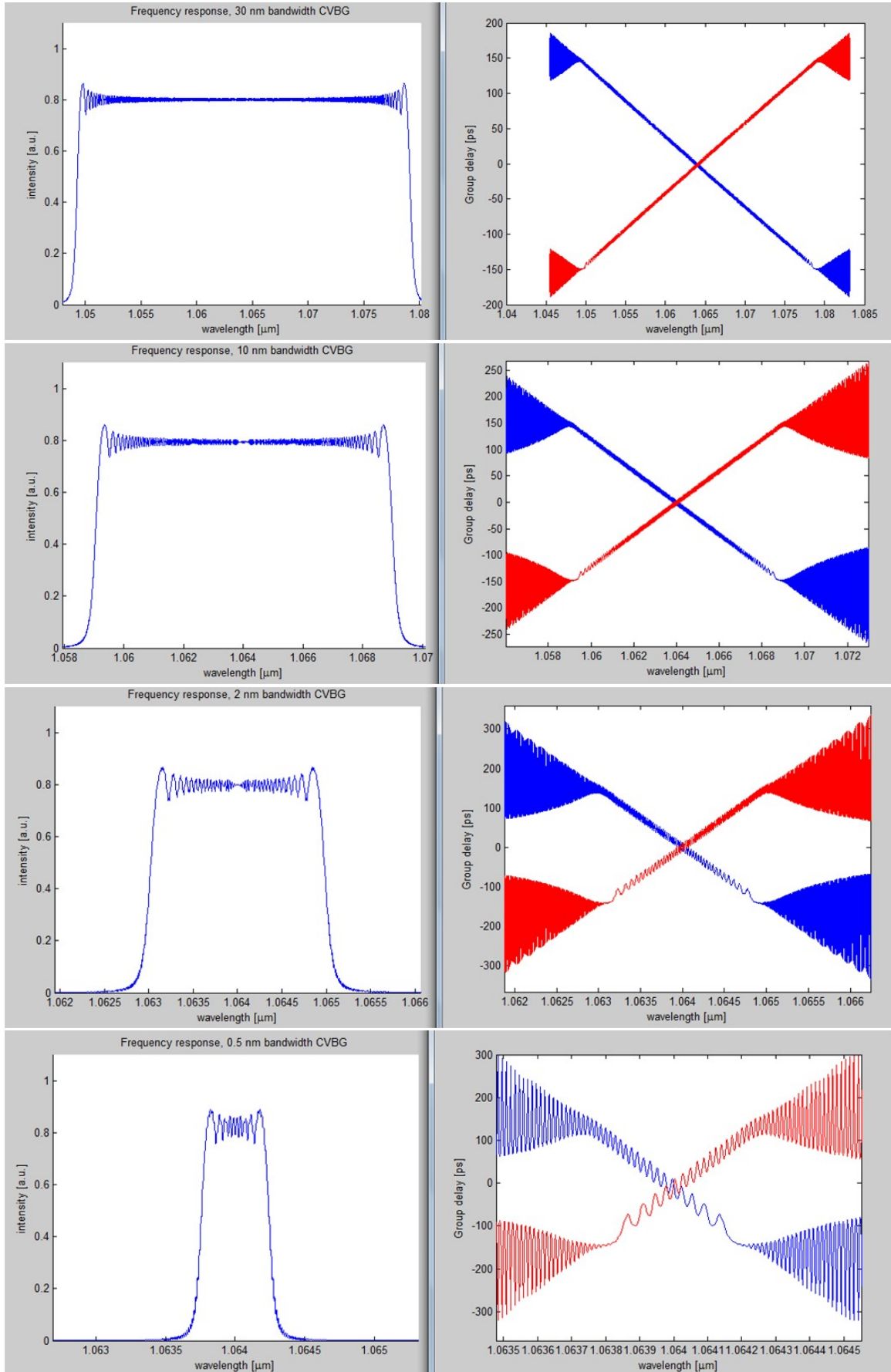
Figure 5.1: Frequency responses for 3 cm long, 80 percent efficient CVBGs for various bandwidths
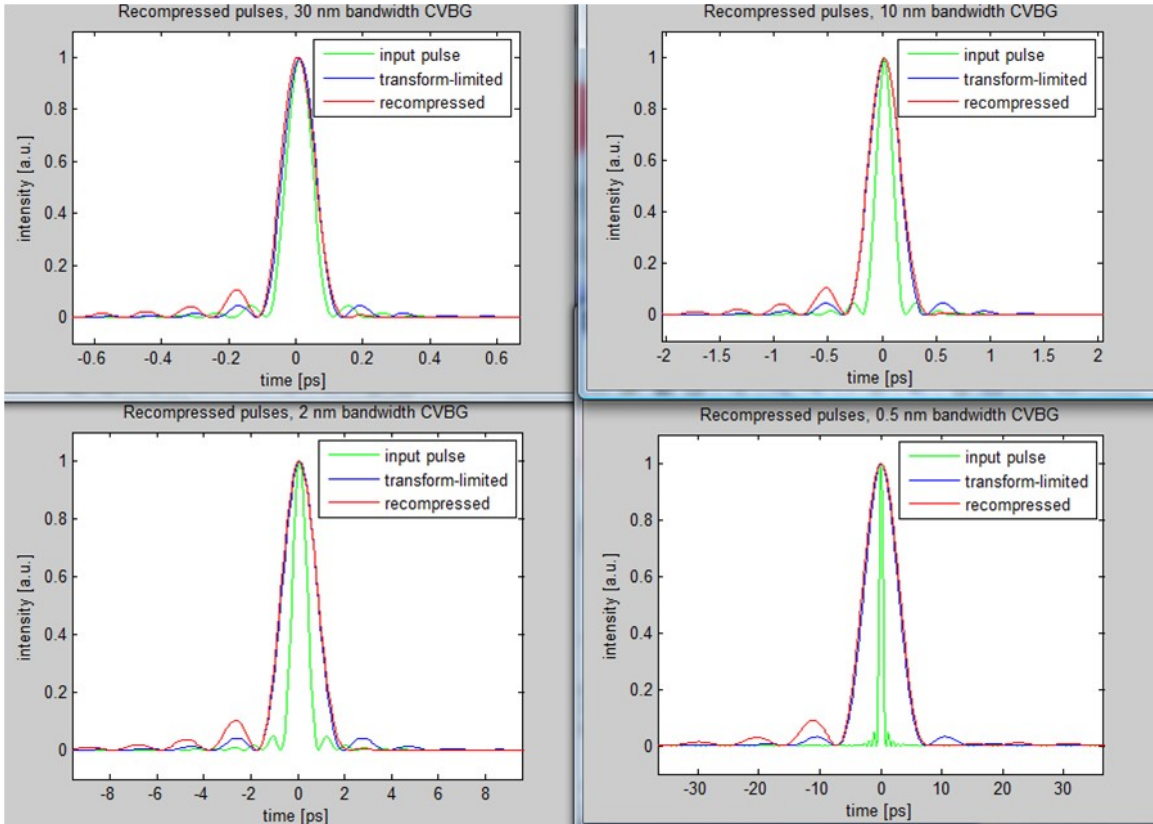
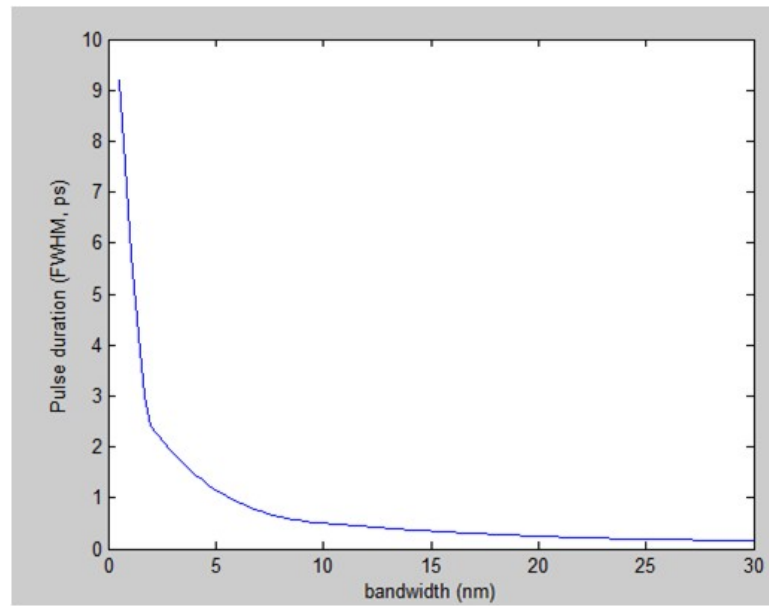Figure 5.2: Corresponding recompressed pulses to Fig. 5.1

Figure 5.3: Recompressed pulse duration (FHWM) vs bandwidth

The next question that arises is whether altering the length can be a means of ameliorating the pulse distortion for the narrow-bandwidth CVBGs. Figure 5.4 plots the frequency responses of several CVBGs of varying lengths with bandwidths of 1 nm and reflectivities of again 80%.

The simulated responses in Figure 5.4 show that the ripple scales in proportion to the length of the CVBG. As a consequence, when choosing design parameters for a CVBG stretcher/compressor device for a CPA system, a balance must be met between longer gratings, yielding less amplifier nonlinearity due to the less intense stretched pulses, and shorter gratings, yielding better temporal reciprocity. This can be accomplished in a straight-forward manner by computing the self-phase-modulation induced dispersion of a highly chirped pulse, via the method presented in [59], and weighing it against the computed transfer function using the analytic theory presented in [48].

As detailed in [60], the ripple also scales with the depth-of-index modulation Δn. Accordingly, higher reflectivity will result in degraded reciprocity. Moreover, increasing the bandwidth of a grating with a fixed length will need a correspondingly stronger Δn to maintain the same reflectivity. Fortunately, as was previously observed, increasing the bandwidth also decreases the magnitude of the group delay ripple. Generally, the ripple is proportional to LΔn/B, where L is the CVBG length and B is the bandwidth. Figure 5.5 shows the ripple for a 1 nm bandwidth and a 5 nm bandwidth CVBG both of 3 cm in length for various Δn (a), with the reflectivity spectra plotted in (b).

For high energy CPA applications, such as X-ray generation via solid-target interaction, the pulse contrast is a critical factor. When the prepulse intensity reaches the ionization threshold for the target, typically $10^9 - 10^{10} \, W/cm^2$ for solids, a pre-
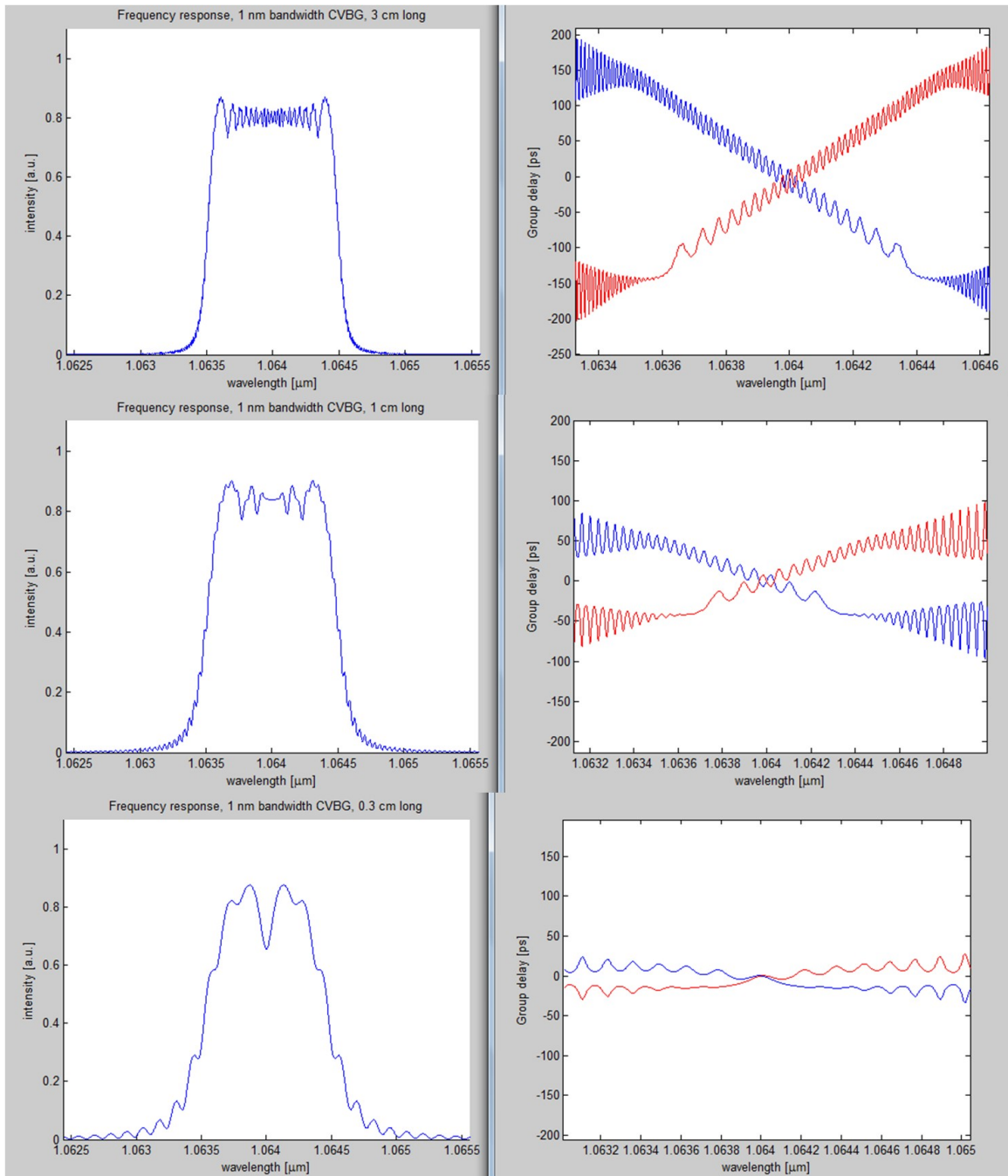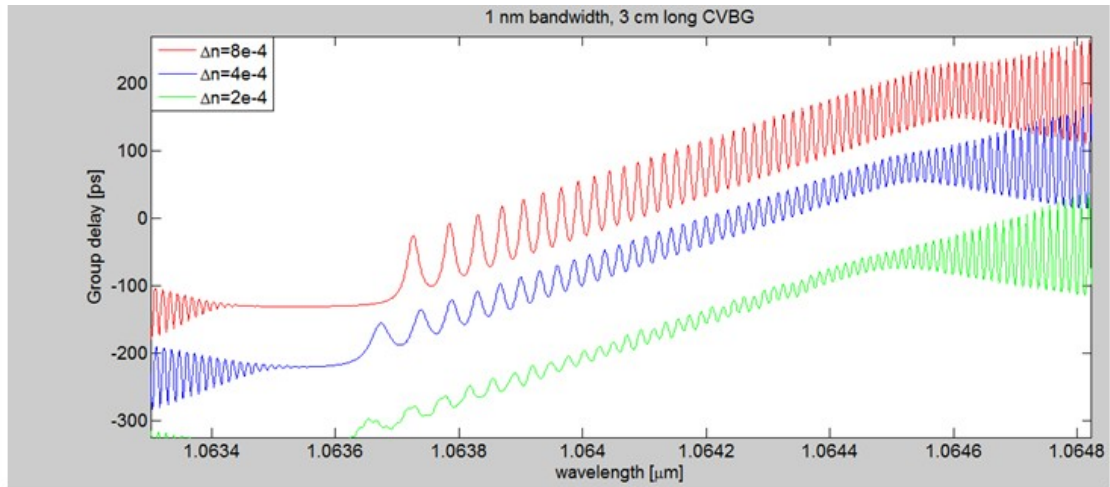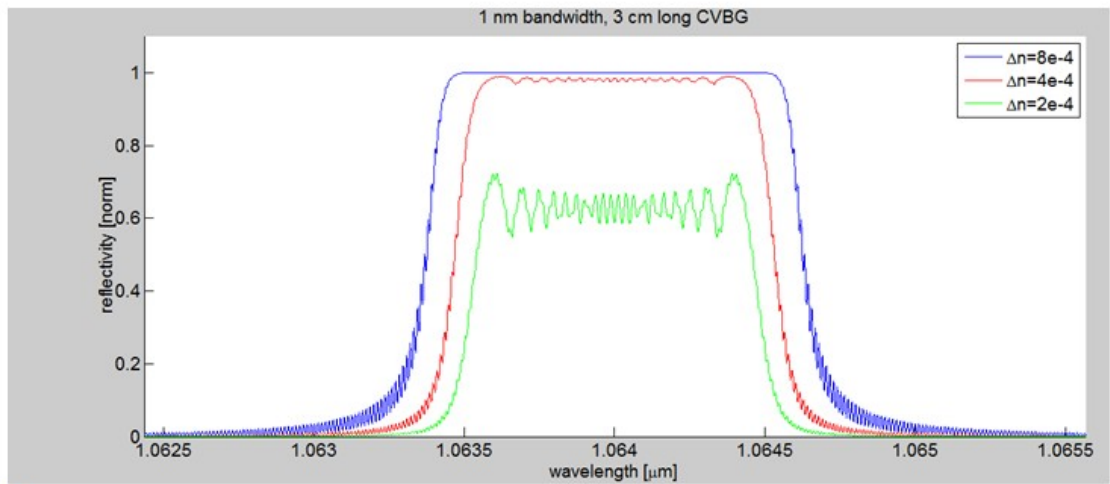
Figure 5.4: Frequency responses of several CVBGs of varying lengths with bandwidths of 1 nm and reflectivities of 80%

Figure 5.5: CVBG response for varying Δn

plasma is created the will perturb the target before the main pulse arrives. If for example, a millijoule pulse is needed and the peak intensity will reach $10^{16} \, W/cm^2$, the contrast between the pulse to the prepulse must be 70 dB or greater. Dorrer et al [58] demonstrated that the pulse pedestal intensity scales quadratically with the phase ripple for short pulses. This means that for such demanding applications, a high degree of reciprocity is absolutely necessary. Again it is noted that greater bandwidths yield smaller ripples and hence enhanced recompressed pulse quality. A log-scale comparison of recompressed pulses for 3 cm long CVBGs each with a 90% reflectivity for 10, 25, and 50 nm of bandwidth is shown in Figure 5.6. The input spectra are taken to be Gaussian with a 10 nm FWHM.

Since energetic CPA applications typically benefit from shorter pulse durations (few-hundred to few-tens of femtoseconds), broad-bandwidth CVBGs can be used for the stretchers and compressors and deliver high compression fidelity with high pulse contrast (the 50 nm bandwidth for example has an > 80 dB contrast ratio shown in Figure 5.6).

5.4   Experiment and Comparison to Theory

To confirm the validity of the previous analysis, the computed recompressed pulses are benchmarked against pulses from an experimental Yb-fiber-CPA system using current CVBG stretchers and compressors. Figure 5.7 illustrates the experimental setup. 100 fs pulses from a Nd:Glass oscillator are stretched and recompressed by the same CVBG. The polarization independence of the CVBGs allows for simple extraction of the reflected beams via waveplates and beamsplitters. The resulting spectra and autocorrelations for the compressed pulses are then measured. A small displacement is used to avoid crosstalk between the stretched and compressed beams.
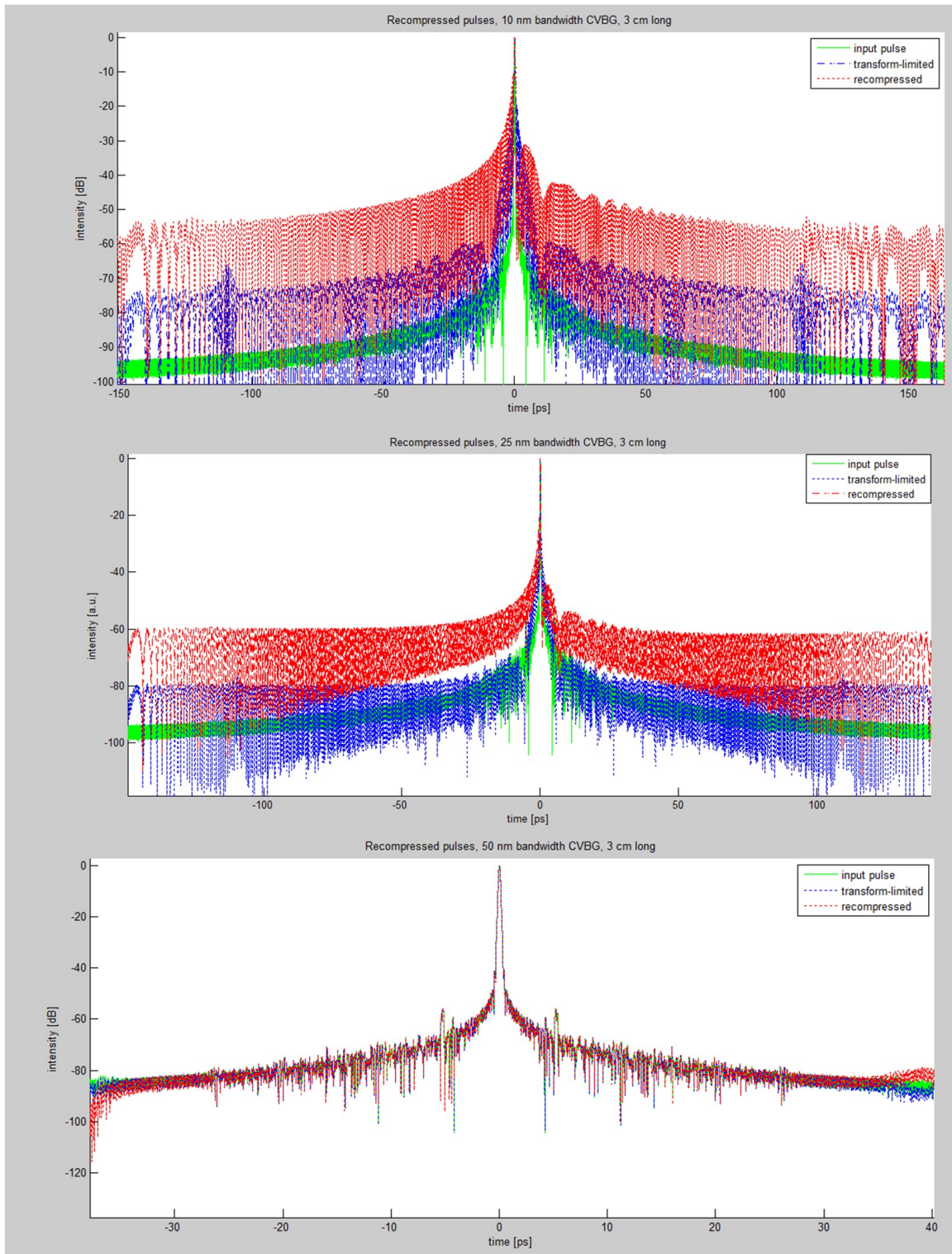
Figure 5.6: High dynamic range calculations for recompressed CVBG pulses for various bandwidths
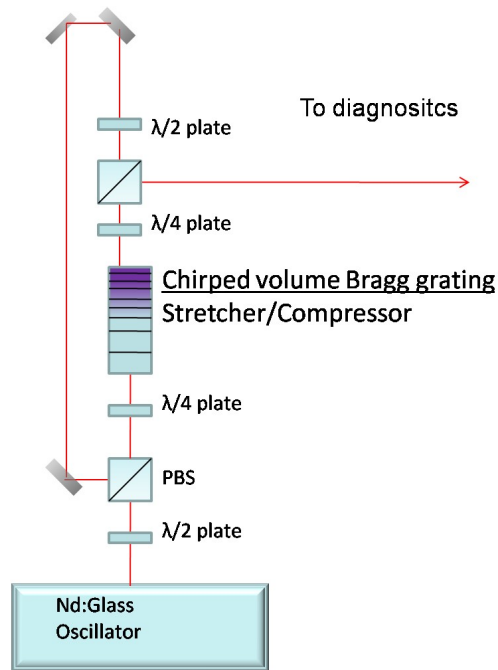
Figure 5.7: Reciprocity measurement setup

CVBGs of bandwidths of 27, 7, 4, and 0.9 nm centered at 1064 nm with reflectivities of 65 percent, 75 percent, 75 percent, and nearly 100 percent, respectively, are tested. All gratings are 3 cm in length.

Figure 5.8 shows the resulting autocorrelation traces, along with the transform-limited autocorrelations computed from the zero-phase FFT of the measured spectra as well as the autocorrelations predicted by the analytical theory. In all cases, the measured autocorrelations agree well with theory. Most notable are the extreme cases of 27 nm bandwidth (a), in which the recompressed pulses are transform-limited with 180 fs durations, and the high reflectivity, narrow-band 0.9 nm case (d), in which the pulses deviate significantly from the transform-limit. This can be explained by the group-delay ripple, which is negligible for 27nm grating (see Fig. 5.1) but quite strong for the latter due to strong interference effects from the high index-modulation and strong chirp.

The good agreement between measurement and computation validates the models
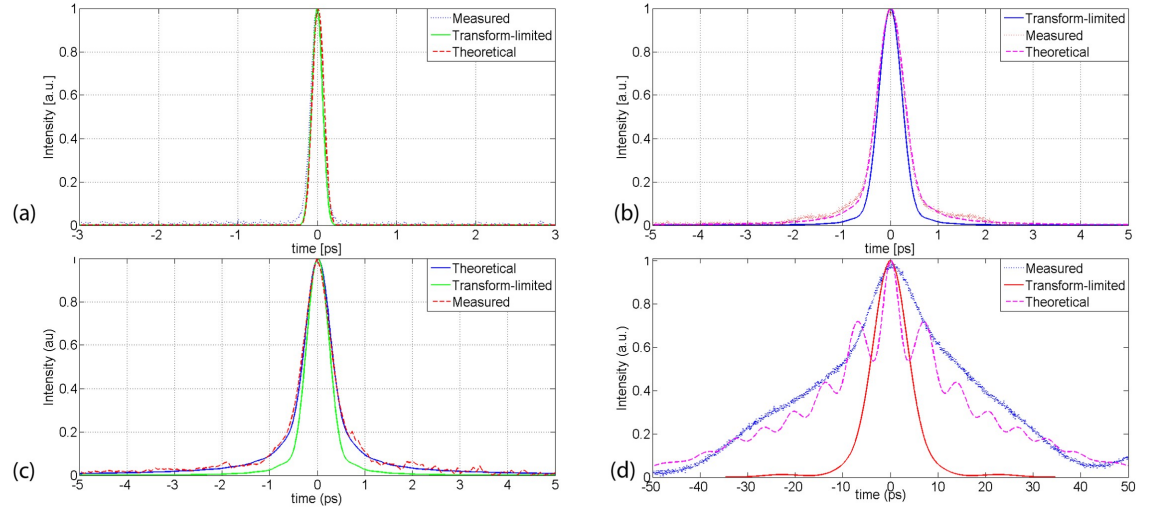
Figure 5.8: Measured autocorrelations compared to transform-limits and theory for (a) 27 nm, (b) 7 nm, (c) 4 nm, and (d) 0.9 nm bandwidth CVBGs

and moreover demonstrates the profound effect of bandwidth on reciprocity. As the recompressed pulses are several times the transform-limit for the narrow-bandwidth grating, these will generally need to be enhanced to be usable for most applications. The broadband 27 nm (180 fs) CVBG produces recompressed pulses that are transform-limited within measurement error indicating its viability. High dynamic-range measurements are the next step to evaluate the recompressed pulse quality.

5.5   Apodization

Apodization, or removing the foot of the device by tapering the index modulation towards the edges, is an established technique for mitigating group delay ripple [61] as it eliminates the interference caused by the index discontinuities when the beam enteres the gratings. For most ultrafast applications, the performance of the unapodized CVBGs is nearly transform-limited as demonstrated in Section 3. However, in the cases of high-energy applications that require high pulse contrast and for narrow bandwidth picosecond CPA with high efficiency, it is necessary to reduce
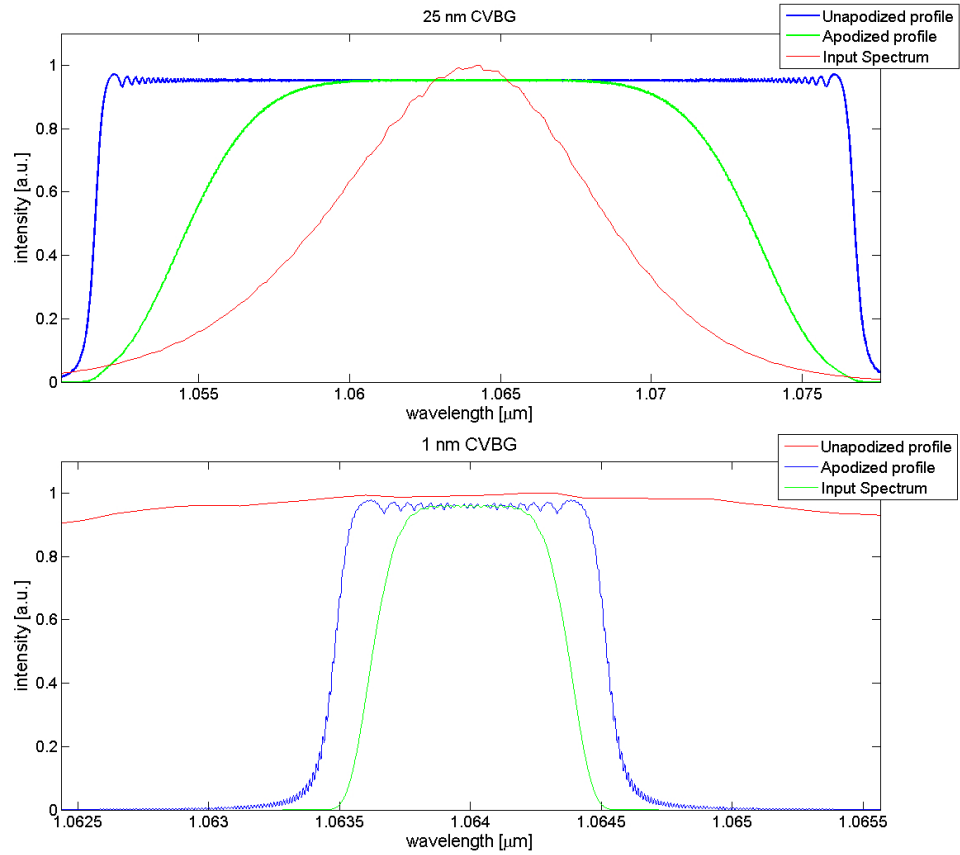
Figure 5.9: CVBG spectral profile comparison with and without apodization

the group delay ripple in order to achieve usable recompressed pulses.

These two cases are considered numerically using the transfer-matrix method (TMM) with cosine apodization as described in [43]. A 25 nm CVBG 3 cm in length with 95% efficiency and a 1 nm CVBG 3cm in length with 95 percent efficiency are evaluated with and without apodization. Figure 5.9 shows the reflectivity profiles, Fig. 5.10 shows the group delays, and Fig. 5.11 shows the recompressed pulses on a log scale. The plots clearly indicate the benefits of apodization in the group delay ripple and the temporal contrast.
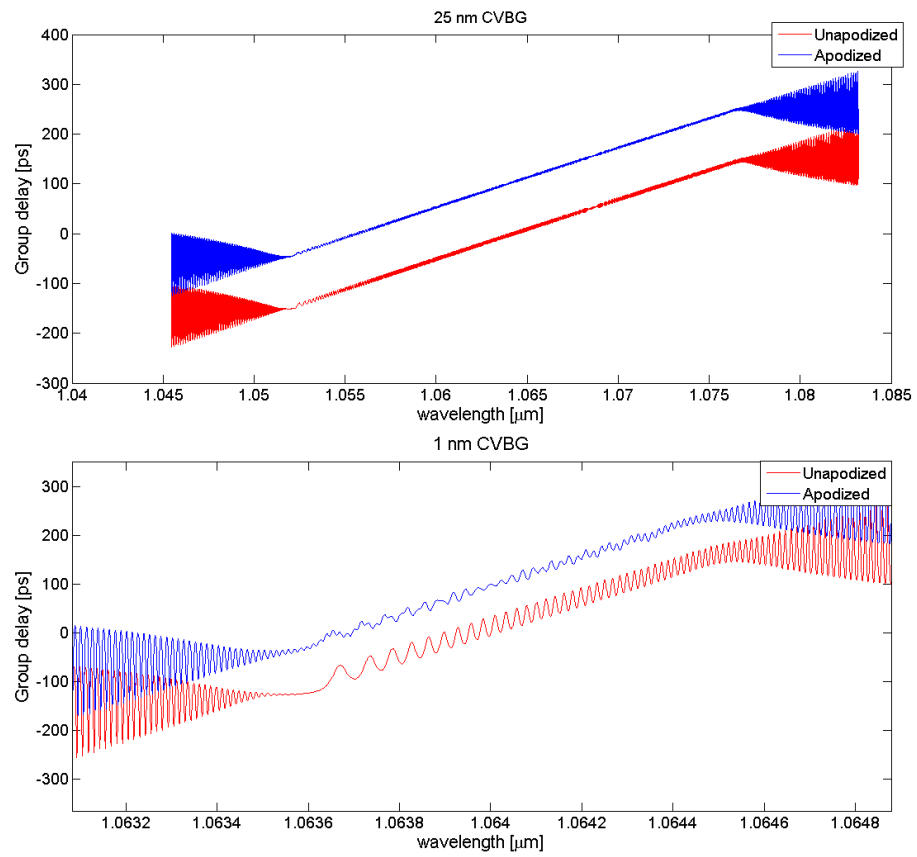
Figure 5.10: CVBG group delay response comparison with and without apodization
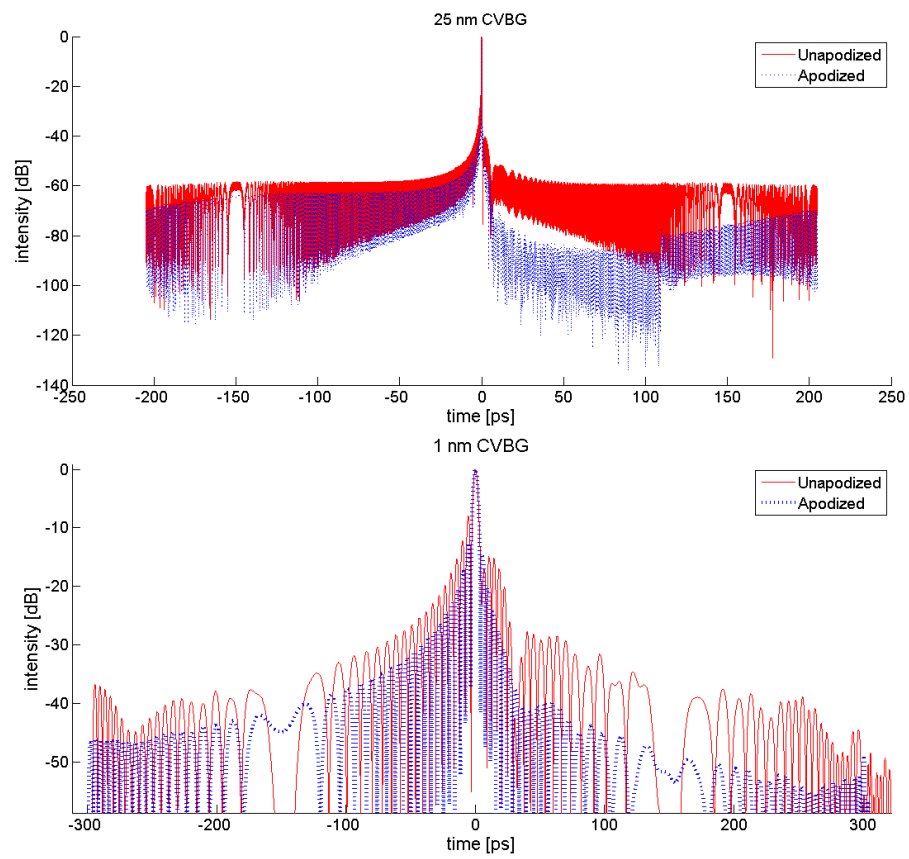
Figure 5.11: CVBG recompressed pulse comparison with and without apodization

5.6 Conclusion

In this work, the effects of non-reciprocal group delay ripple in chirped-volume-Bragg-grating stretchers and compressors is evaluated numerically and experimentally. It is shown that the recompressed pulse durations remains nearly unchanged for broadband (sub-ps) pulses but degrades for narrow-band (1 nm or less), high-reflectivity (> 95%) cases. When high-contrast is needed, such as in high-field solid target experiments, GDR reduction is needed to reduce the pedestal even in the broadband cases. Apodization, or tapering off the refractive index modulation at the CVBG ends, is shown to eliminate the GDR resulting in high-contrast, transform-limited recompressed pulses regardless of the bandwidth, length, and reflectivity of the CVBG.

CHAPTER VI

Energy Scaling in a Chirped Volume Bragg Grating based Yb-fiber CPA System

The viability of using chirped volume Bragg gratings for mJ-scale CPA systems is demonstrated. A CVBG-based fiber-CPA system with 0.4 mJ amplified and 290 μJ recompressed energy from a CVBG compressor is reported.

6.1 Introduction

Ultrafast high power fiber chirped pulse amplification (CPA) lasers are promising for a wide range of applications including material processing and inspection, THz imaging, and EUV and X-ray generation. For practical systems, however, conventional diffraction grating based stretchers and compressors cannot be used due to their size and alignment complexity. Chirped volume Bragg gratings (CVBGs) made of photo-thermo refractive (PTR) glass are novel devices that have the properties compatible with keeping fiber CPA systems compact and robust. With only a few centimeters of length, a CVBG can stretch a pulse to hundreds of picoseconds, enabling the amplification of pulses to high energies in a fiber amplifier while avoiding damage and mitigating nonlinear effects [55, 62]. Such long stretched pulses and, consequently, high pulse energies are not achievable with any other compact pulse stretching and compressing technology. Previously [63, 64] we have demonstrated
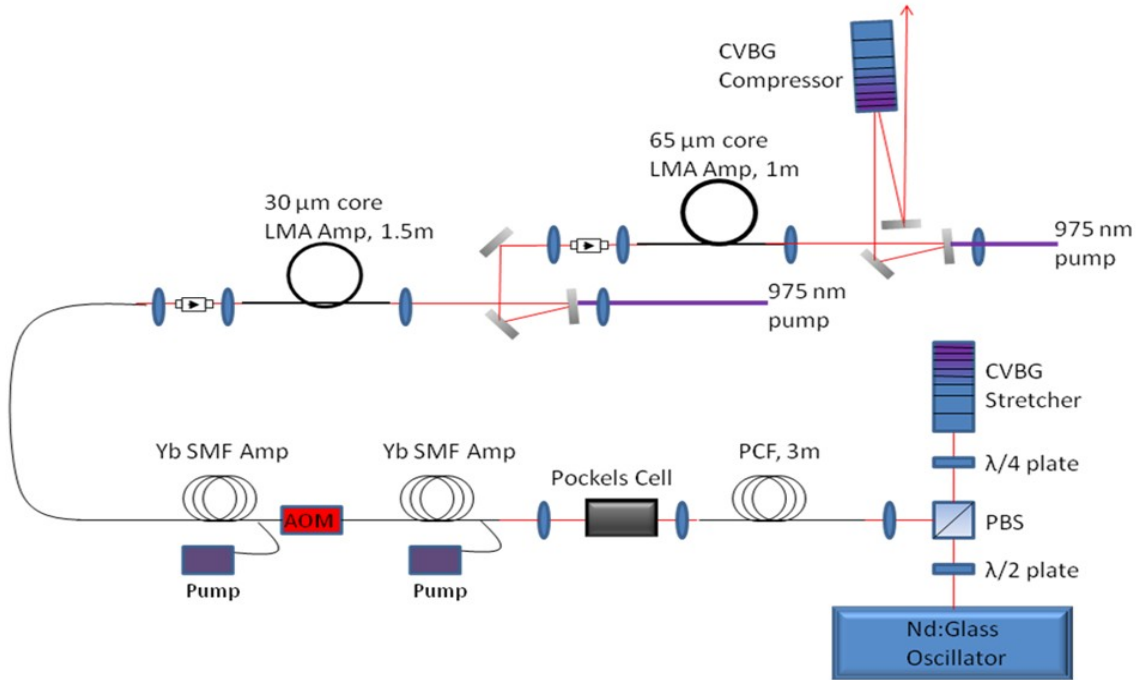
Figure 6.1: Experimental setup for the CVBG-based fiber-CPA system

picosecond and femtosecond CVBG-based FCPA with average power scaling into the 50-100 W power range, thus proving practicality and the great power scaling potential of this technology.

In this work we explore pulse energy scaling of CVBG pulse compressors. Using a 31 mm long and 5 nm bandwidth (centered at 1064 nm) CVBG grating, which provides spatial-chirp free and 75% compressed-pulse reflection efficiency, we demonstrate up to 400 μJ extraction with 310 ps stretched pulses from a 65 μm core fiber amplifier. After the CVBG compressor, this yields 290 μJ pulses. Compression down to 1.2 ps duration has been achieved.

6.2   Experiment and Results

The experimental setup is shown in Fig. 6.1. A mode-locked Nd:Glass oscillator outputs a train of 110 fs pulses at 72 MHz with a central wavelength of 1064 nm.

These pulses are then stretched to 310 ps in a CVBG arranged for positive dispersion. Note that the bandwidth is reduced to 5 nm at this point due to the reflectivity window of the grating. A Pockels cell with a 10ns time window is then used to reduce the repetition rate to 1 kHz. The pulses are then injected into a single-mode Yb-doped fiber amplifier, which is spliced to an acousto-optic modulator (AOM) with a 100 ns time window to maintain a negligible ASE background after amplification in all stages. After the AOM, the pulses enter another single-mode fiber amplifier which brings the pulse energy to 400 nJ. Two power amplifiers are used to obtain high energy. The first is a 1.5 m long 30 μm core diameter Yb-doped fiber which brings the pulse energy to 10 μJ. Following that is a 1 m long 65 μm core diameter Yb-doped fiber which brings the energy as high as 0.4 mJ. A 3 m long air-core photonic-crystal fiber with negative dispersion was used at the input to balance the positive dispersion of the rest of the fiber-optic path.

A CVBG, with a 75% reflection efficiency, oriented for negative dispersion is used to recompress the pulses to ultrashort durations. Note that the dispersions of the oppositely oriented CVBGs negate each other, leaving the residual net dispersion of the amplifier fibers and air-core PCF dispersion compensator. The spectrum at the output of the compressor grating measured at 0.4 mJ of pulse energy is shown in Fig. 6.2(a). After compression, energies of up to 290 μJ have been achieved. Fig. 6.2(b) shows the measured autocorrelation trace, corresponding to a 1.2 ps pulse duration. This duration is still limited by the incomplete dispersion compensation in the current experimental setup of the linear and higher-order dispersion components as well as self-phase modulation induced dispersion. Work is in progress in achieving optimized dispersion compensation using careful dispersion matching of the fiber-optic path using positive and negative dispersion fibers.
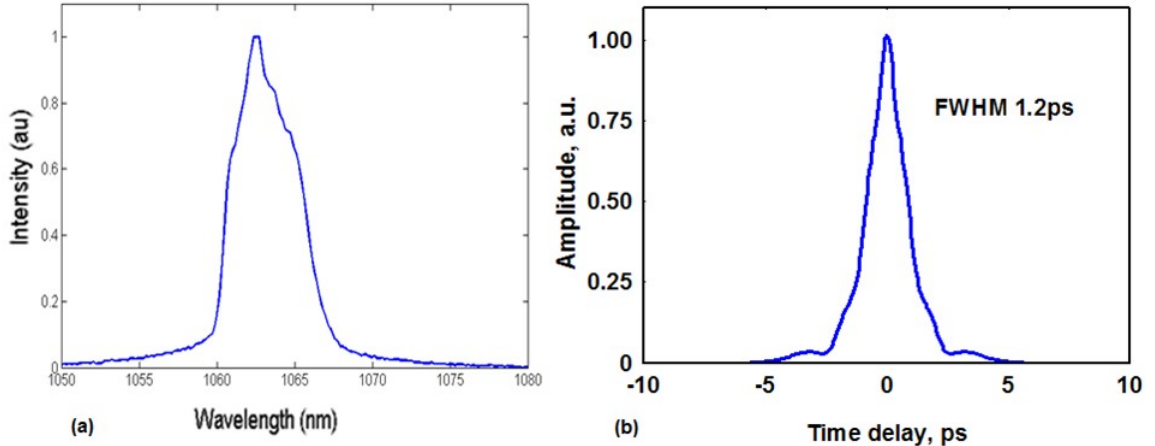
Figure 6.2: (a) Spectrum at the output of the CVBG measured with 0.4 mJ of injected energy (b): Measured autocorrelation trace of 1.2 ps compressd pulse

In previous experiments, the CVBGs available suffered from spatial-chirp caused by aberrations in the writing process. As a result, the output beams were not diffraction limited and part of the bandwidth would be lost when coupling into fibers. Recent advances in the grating fabrication process have allowed for nearly spatial-chirp free CVBGs. Figure 6.3(a) shows the spatial-tilt fan measurement for the gratings used in the current experiment. The gratings are tilt-free within measurement accuracy. The nearly diffraction-limited output beam, measured with a pulse that fills the gratings spectral window, is shown in Fig. 6.3(b), indicating that nearly diffraction-limited beam quality of 65 μm core fiber amplifier output ($M^2 < 1.1$, see [25, 65]) has been preserved after the compressor.

6.3   Discussion and Conclusion

We have demonstrated that CVBG pulse compressors have potential for FCPA pulse energy scaling into the mJ range. In only 3.1 cm of length, the CVBG can stretch a pulse to 310 ps wide, mitigating the nonlinear effects from propagating in the fiber amplifiers. Our system produced pulses of 0.4 mJ, limited by the fiber
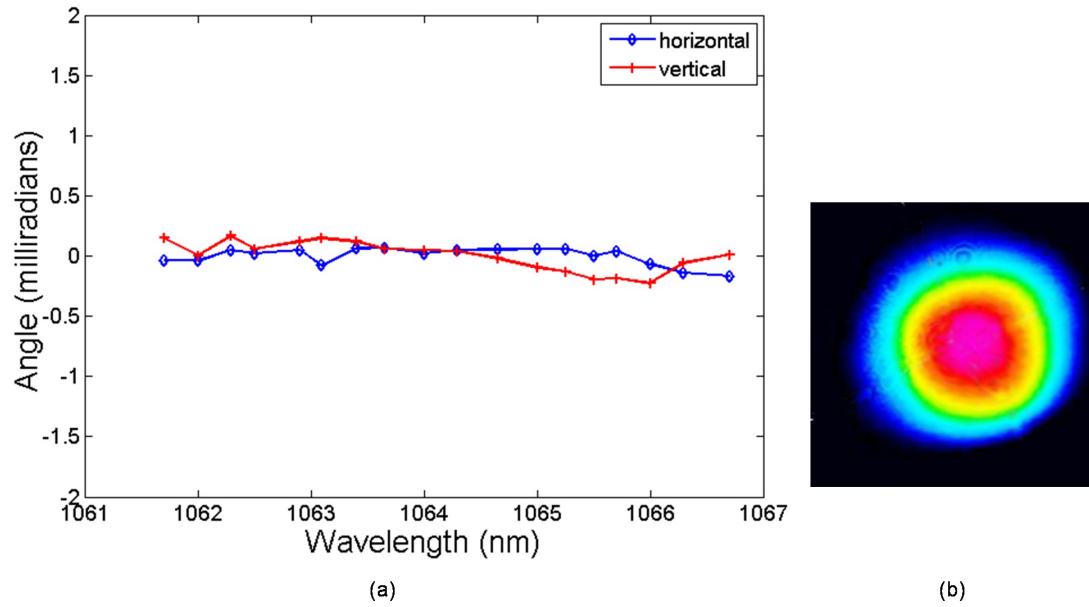
Figure 6.3: (a) Spatial tilt-fan of the grating used in experiment; (b): Beam at the output of the CVBG, with the spectral window filled

amplifier, which were recompressed with a 75% efficiency. The currently achieved 1.2 ps pulses are longer than the bandwidth limit for the 5nm bandwidth CVBG spectral window used in this experiment. We anticipate that with further work optimum compensation for the fiber dispersion will be achieved and the bandwidth limited duration of 400 fs will be approached. Longer gratings (10 cm) are under development that will enable us to stretch the pulses to 1 ns, allowing for further energy scaling to mJ pulses with safe amplification.

CHAPTER VII

Vacuum-free Hard X-rays Driven by High-Field Pulses from a Femtosecond Fiber Laser

7.1   Introduction

A compact, vacuum-free hard X-ray source based on high-field pulses from a femtosecond fiber laser interacting with nickel in gently flowing helium is demonstrated. The K_α X-ray energy conversion efficiency is $1.7\mathrm{x}10^{-9}$. This is a proof-of-principle experiment illustrating the viability of using fiber-CPA lasers for high-field physics experiments.

7.2   Laser Setup

Figure 7.1 illustrates the laser setup. A mode-locked Nd:Glass oscillator outputs a train of 110 fs pulses at 72 MHz with a central wavelength of 1064 nm. A Martinez-design positive dispersion stretcher [22] brings the pulse duration to 1 ns. A Pockels cell with a 10ns time window is then used to reduce the repetition rate to 1 kHz. The pulses are then injected into a single-mode Yb-doped fiber amplifier, which is spliced to an acousto-optic modulator (AOM) with a 100 ns time window to maintain a negligible ASE background after amplification in all stages. After the AOM, the pulses enter another single-mode fiber amplifier which brings the pulse energy to 400 nJ. Two power amplifiers are used to obtain high energy. The first is a 1.5 m long 30
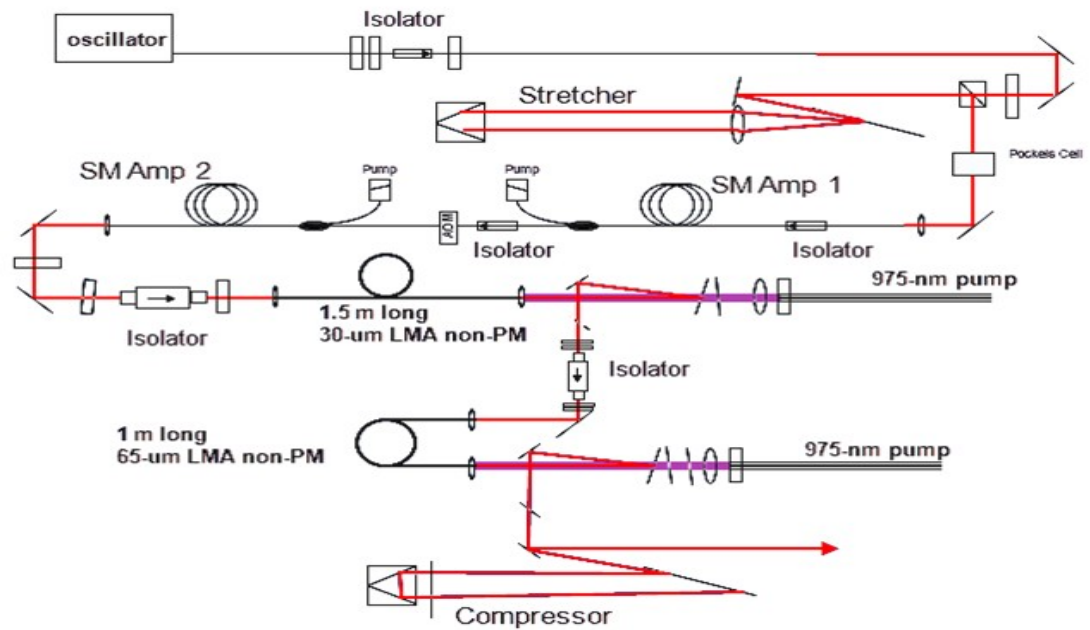
Figure 7.1: High energy FCPA laser setup

μm core diameter Yb-doped fiber which brings the pulse energy to 10 μJ. Following that is a 1 m long 65 μm core diameter Yb-doped fiber which brings the energy as high as 0.15 mJ. The pulses are compressed down to 400 fs by a folded one-grating Treacy compressor [21].

7.3 Experimental Setup and Results

Figure 7.4 illustrates the setup for laser X-ray generation. An F/2.3 lens focuses the beam onto a polished, rotating nickel target with s-polarization. A tube delivers helium just in front of the target in order to minimize plasma generated wavefront distortions to the delivered pulse. With the given laser parameters, an intensity of 7.1×10^{15} W/cm^2 is generated. An X-ray spectrometer is used to characterize the emission, while a visible spectrometer is used to minimize the nitrogen ionization.

Figure 7.5 shows the resulting X-ray spectrum. Nickel Ka X-rays are evident from
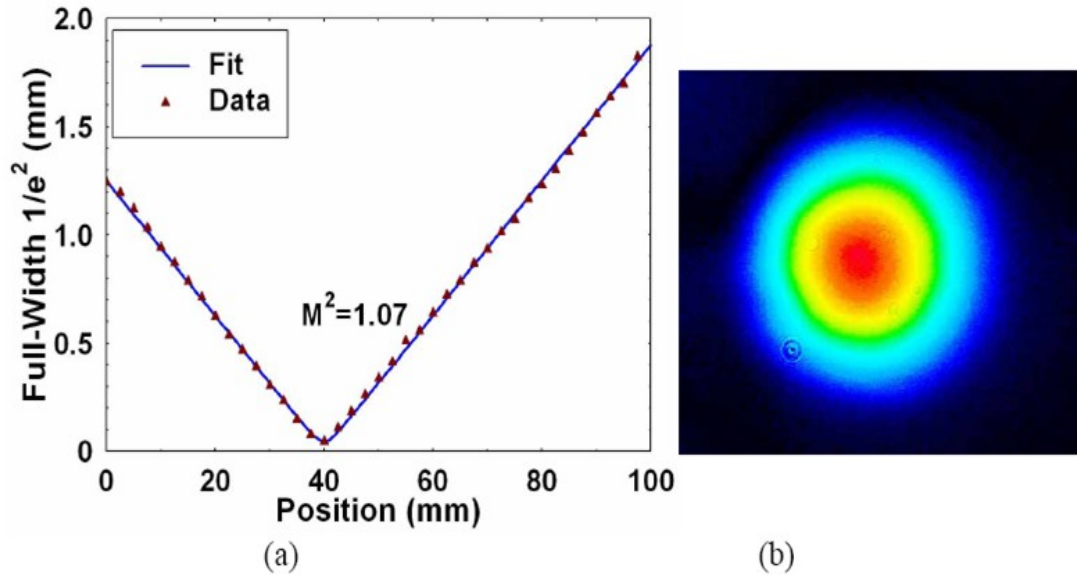
Figure 7.2: (a). Beam quality measurement of the 65-μm-core VLMA fiber using the knife-edge method with a 75-mm focusing lens. The curve fit of the measured data shows the beam has an M^2=1.07. (b). Beam profile measurement with a collimated beam using a CCD camera showing a symmetrical LP_{01} mode profile with FWHM 2-mm diameter.
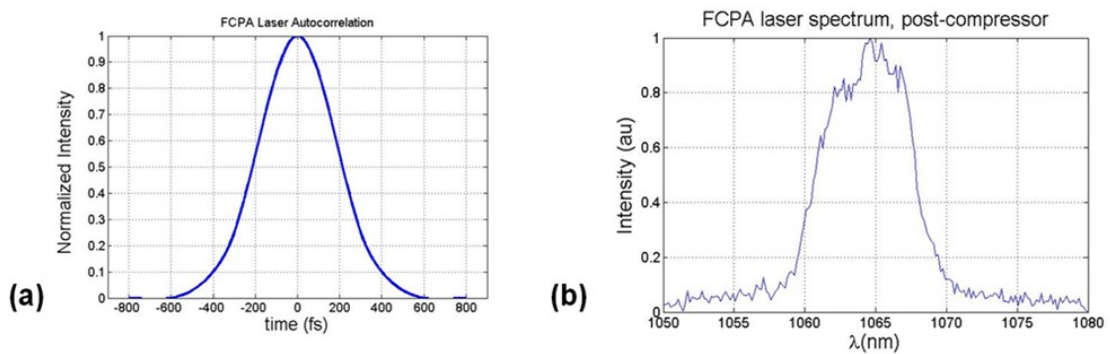
Figure 7.3: (a) Autocorrelation of the compressed laser output, showing a 400 fs FWHM (1.41 deconvolution factor) pulse, close to the transform limit. (b) Spectrum at the output of the FCPA laser.
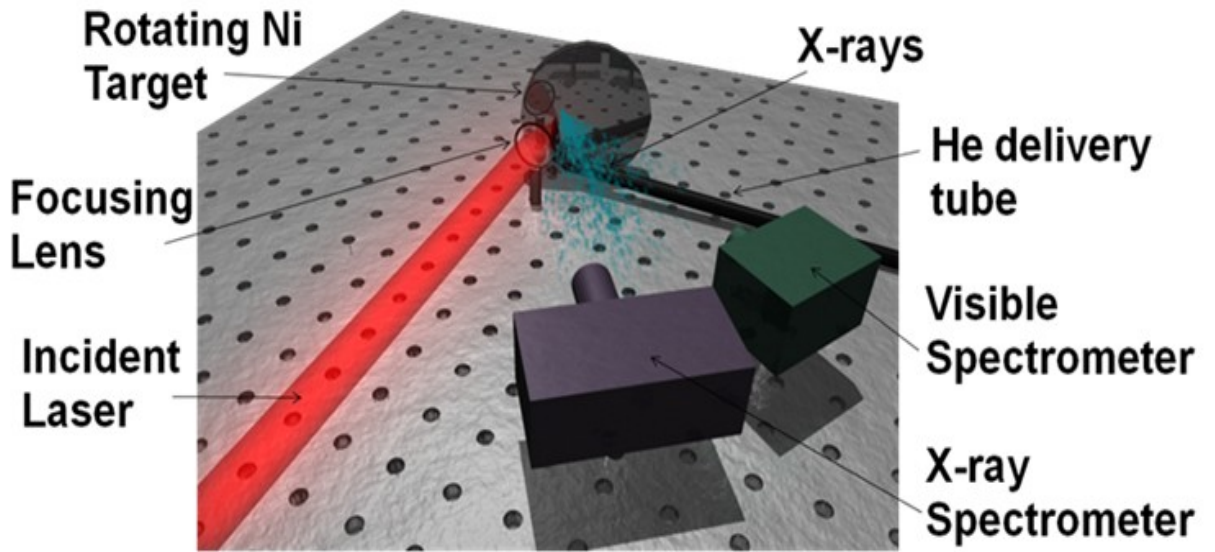
Figure 7.4: X-ray generation setup
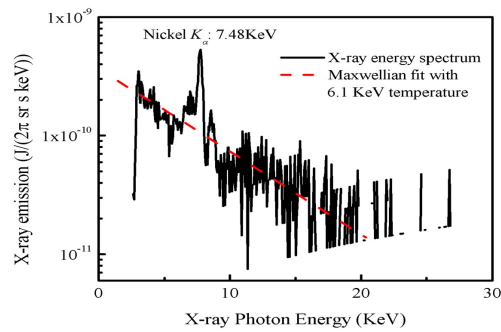
Figure 7.5: Nickel X-ray spectrum

the measured spectrum. The K_α X-ray photon flux is 2.2×10^5 photons per second per 2π sr in front of the target. This corresponds to an energy conversion efficiency of 1.7×10^{-9}.

CHAPTER VIII

Conclusion

Ultrafast high power fiber chirped pulse amplification (CPA) lasers are promising for a wide range of applications including material processing and inspection, THz imaging, and EUV and X-ray generation. Fiber lasers are particularly attractive over conventional bulk solid-state lasers due to their potential to be made compact, since the amplifiers can be coiled, monolithic, since the components can be spliced together, and hence robust since there would be no free-space components requiring alignment. Moreover, fiber lasers can produce diffraction-limited beams even at high power due to the lack of thermal aberration. However, several challenges still need to be overcome in order for fiber CPA lasers to reach their full potential for robustness and compete with bulk crystal lasers in terms of pulse energy.

Firstly, current fiber CPA systems still rely on conventional bulk grating stretchers and compressors, which are large and complex to align. This is incompatible with keeping fiber lasers compact and monolithic. A promising alternative to these systems are chirped volume Bragg gratings (CVBGs), which are slabs of glass of centimeters dimensions that can stretch and recompress ultrashort pulses with only a few nanometers of bandwidth to hundreds of picoseconds depending on their length (the chirp-rate is 100 ps/cm). This is accomplished by writing a longitudinal index

of refraction profile into photothermo-refractive (PTR) glass in such a way that the Bragg wavelength varies linearly with position. A positive dispersion can be applied to the pulse by sending it in one way, and a reciprocal negative dispersion can be applied by sending the pulse into the opposite end of the CVBG. Due to their small size and trivial alignment, CVBGs are compatible with keeping fiber CPA lasers compact and robust. Furthermore, the excellent thermal properties of PTR glass enable CVBGs to withstand high average laser powers.

The next major challenge for fiber lasers is the development of large core area fibers that can handle high energy with minimal nonlinearity, but still provide single-mode, diffraction-limited output beams. Single-mode operation is important for lasers due to the desire to obtain the minimum spot-size for maximum intensity, and it is even more essential for ultrafast lasers since modal dispersion will result in temporally broadened pulses. Conventional large-mode-area fibers (tens of m in diameter) can withstand high energies, however, as the core size increases, robust single-mode operation becomes nearly impossible. There are several proposed technologies to overcome this limitation including PCF rods, leakage-channel fibers, and forced higher-order mode operation of LMA fibers. These have the disadvantages of limited robustness and compactness (the PCF rods cannot be coiled) as well as the lack of ability to be spliced. The most promising new technology however is chirally-coupled-core (CCC) fibers, which are essentially LMA fibers that have a smaller helical core wrapped around the main core, which preferentially couples higher-order modes out. The result is an effectively single-mode fiber with a large mode area. Some major advantages CCC fibers have over PCF rods is that they can be bent, making it possible to keep the amplifiers compact, and they can be spliced, allowing for monolithic architectures.

The primary objectives of this thesis are further average power and energy scaling of fiber-CPA systems while still maintaining compactness and robustness and ultrashort pulse durations. Chirped volume Bragg gratings and chirally-coupled core fibers are expected to be the basis for this further scaling. However, there are issues that need to be dealt with before these technologies can be utilized in commercial systems. The issue of spatial chirp in CVBGs for example, must be analyzed for the production of usable gratings. Thermal and nonlinear effects in the gratings must be modeled accurately in order to design a system that mitigates these effects as much as possible, as well as to know the fundamental limitations.

This thesis describes the current state of development of fiber-CPA systems. Experiments on energy and power scaling are described, and the results will be presented. The present limitations of thermal distortion in CVBGs are discussed, and an analysis modeling the thermal effects on recompression are given. Other limitations, such as nonlinearity are explored and solutions proposed. An important application of fiber-CPA, namely X-ray generation, are demonstrated.

8.1   Outlook

Chirped volume Bragg gratings and chirally-coupled core fibers have shown great potential for scaling fiber CPA laser systems to high average powers and for reaching high energies with short pulse durations all while providing the potential for compact, robust systems with monolithic architectures. Several challenges still remain for utilizing these technologies to their full potential. A more detailed thermal analysis needs to be carried for CVBGs that can accurately match experimental results, which will most likely require a finite-element analysis. Current calculations indicate that with water cooling, CVBGs will be suitable for systems approaching a kilowatt

of average power, but the ultimate limit is still unknown. The effects of nonlinearity within CVBGs need to be investigated in order to know what energies can be withstood before SPM and self-focusing become overly detrimental. Careful system design, including optimizing fiber lengths and pump powers, is necessary to reach peak energies while balancing the effects of nonlinearity. Higher powers and energies can be expected as CVBGs are made longer (for increased stretched pulse durations) and CCC fibers with larger core areas can be manufactured.

BIBLIOGRAPHY

BIBLIOGRAPHY

[1] N Matuschek, FX Kartner, and U Keller. Exact coupled-mode theories for multilayer inter-ference coatings with arbitrary strong index modulations. *IEEE JOURNAL OF QUANTUM ELECTRONICS*, 33(3):295–302, MAR 1997.

[2] Michael Craig Swan, Dissertation, University of Michigan, 2008.

[3] Chi-Hung Liu, Dissertation, University of Michigan, 2007.

[4] D STRICKLAND and G MOUROU. COMPRESSION OF AMPLIFIED CHIRPED OPTI-CAL PULSES. *OPTICS COMMUNICATIONS*, 55(6):447–449, 1985.

[5] Gerard A. Mourou, Toshiki Tajima, and Sergei V. Bulanov. Optics in the relativistic regime. *Rev. Mod. Phys.*, 78(2):309–371, Apr 2006.

[6] PM Paul, ES Toma, P Breger, G Mullot, F Auge, P Balcou, HG Muller, and P Agos-tini. Observation of a train of attosecond pulses from high harmonic generation. *SCIENCE*, 292(5522):1689–1692, JUN 1 2001.

[7] PH Siegel. Terahertz technology. *IEEE TRANSACTIONS ON MICROWAVE THEORY AND TECHNIQUES*, 50(3):910–928, MAR 2002.

[8] Simi A. George, Kai-Chung Hou, Kazutoshi Takenoshita, Almantas Galvanauskas, and Mar-tin C. Richardson. 13.5 nm euv generation from tin-doped droplets using a fiber laser. *Opt. Express*, 15(25):16348–16356, 2007.

[9] Rafael R. Gattass and Eric Mazur. Femtosecond laser micromachining in transparent materials. *Nature Photonics*, 2(4):219–225, 2008.

[10] Daniel Creeden, John C. McCarthy, Peter A. Ketteridge, Timothy Southward, Peter G. Schune-mann, James J. Kmoiak, Webster Dove, and Evan P. Chicklis. Compact fiber pumped tera-hertz source - art. no. 65490P. In Jensen, JO and Cui, HL, editor, *Terahertz for Military and Security Applications V*, volume 6549 of *PROCEEDINGS OF THE SOCIETY OF PHOTO-OPTICAL INSTRUMENTATION ENGINEERS (SPIE)*, page P5490, 1000 20TH ST, PO BOX 10, BELLINGHAM, WA 98227-0010 USA, 2007. SPIE, SPIE-INT SOC OPTICAL EN-GINEERING. Conference on Terahertz for Military and Security Applications V, Orlando, FL, APR 09-10, 2007.

[11] IP Christov, MM Murnane, and HC Kapteyn. High-harmonic generation of attosecond pulses in the ''single-cycle'' regime. *PHYSICAL REVIEW LETTERS*, 78(7):1251–1254, FEB 17 1997.

[12] T. Suedmeyer, C. Kraenkel, C. R. E. Baer, O. H. Heckl, C. J. Saraceno, M. Golling, R. Peters, K. Petermann, G. Huber, and U. Keller. High-power ultrafast thin disk laser oscillators and their potential for sub-100-femtosecond pulse generation. *APPLIED PHYSICS B-LASERS AND OPTICS*, 97(2):281–295, OCT 2009.

[13] Oliver H. Heckl, Rigo Peters, Christian Kränkel, Cyrill R. Baer, Clara J. Saraceno, Thomas Südmeyer, Klaus Petermann, Ursula Keller, and Günter Huber. Continuous-wave yb-doped sesquioxide thin disk lasers with up to 300 w output power and 74% efficiency. In *Advanced Solid-State Photonics*, page AMD1. Optical Society of America, 2010.

[14] Michael O'Connor, V. Gapontsev, V. Fomin, M. Abramov, and A. Ferin. Power scaling of sm fiber lasers toward 10kw. In *Conference on Lasers and Electro-Optics/International Quantum Electronics Conference*, page CThA3. Optical Society of America, 2009.

[15] Chi-Hung Liu, Shenghong Huang, Cheng Zhu, and Almantas Galvanauskas. High energy and high power pulsed chirally-coupled core fiber laser system. In *Advanced Solid-State Photonics*, page MD2. Optical Society of America, 2009.

[16] Tino Eidam, Stefan Hanf, Enrico Seise, Thomas V. Andersen, Thomas Gabler, Christian Wirth, Thomas Schreiber, Jens Limpert, and Andreas Tünnermann. Femtosecond fiber cpa system emitting 830 w average output power. *Opt. Lett.*, 35(2):94–96, 2010.

[17] F. Röser, T. Eidam, J. Rothhardt, O. Schmidt, D. N. Schimpf, J. Limpert, and A. Tünnermann. Millijoule pulse energy high repetition rate femtosecond fiber chirped-pulse amplification system. *Opt. Lett.*, 32(24):3495–3497, 2007.

[18] KO HILL, F BILODEAU, B MALO, T KITAGAWA, S THERIAULT, DC JOHNSON, J ALBERT, and K TAKIGUCHI. CHIRPED IN-FIBER BRAGG GRATINGS FOR COMPENSATION OF OPTICAL-FIBER DISPERSION. *OPTICS LETTERS*, 19(17):1314–1316, SEP 1 1994.

[19] OM Efimov, LB Glebov, LN Glebova, KC Richardson, and VI Smirnov. High-efficiency Bragg gratings in photothermorefractive glass. *APPLIED OPTICS*, 38(4):619–627, FEB 1 1999.

[20] Anne-Laure Calendron, Katrin Wentsch, Joachim Meier, and Max J. Lederer. High power and high energy yb:kyw regenerative amplifier using a chirped volume bragg grating. In *Conference on Lasers and Electro-Optics/International Quantum Electronics Conference*, page CFD2. Optical Society of America, 2009.

[21] E. Treacy. Optical pulse compression with diffraction gratings. *Quantum Electronics, IEEE Journal of*, 5(9):454–458, Sep 1969.

[22] OE MARTINEZ. 3000 TIMES GRATING COMPRESSOR WITH POSITIVE GROUP-VELOCITY DISPERSION - APPLICATION TO FIBER COMPENSATION IN 1.3-1.6 MU-M REGION. *IEEE JOURNAL OF QUANTUM ELECTRONICS*, 23(1):59–64, JAN 1987.

[23] ME Fermann. Single-mode excitation of multimode fibers with ultrashort pulses. *OPTICS LETTERS*, 23(1):52–54, JAN 1 1998.

[24] Jeffrey P. Koplow, Dahv A. V. Kliner, and Lew Goldberg. Single-mode operation of a coiled multimode fiber amplifier. *Opt. Lett.*, 25(7):442–444, 2000.

[25] Kai-Hsiu Liao, Kai-Chung Hou, Guoqing Chang, Vadim Smirnov, Leon Glebov, Rupak Changkakoti, Pri Mamidipudi, and Almantas Galvanauskas. Diffraction-limited 65-um core yb-doped lma fiber based high energy fiber cpa systems. In *Conference on Lasers and Electro-Optics/Quantum Electronics and Laser Science Conference and Photonic Applications Systems Technologies*, page CPDB4. Optical Society of America, 2006.

[26] J. Limpert, A. Liem, M. Reich, T. Schreiber, S. Nolte, H. Zellmer, A. Tünnermann, J. Broeng, A. Petersson, and C. Jakobsen. Low-nonlinearity single-transverse-mode ytterbium-doped photonic crystal fiber amplifier. *Opt. Express*, 12(7):1313–1319, 2004.

[27] Christopher D. Brooks and Fabio Di Teodoro. Multimegawatt peak-power, single-transverse-mode operation of a 100 mu m core diameter, yb-doped rodlike photonic crystal fiber amplifier. *Applied Physics Letters*, 89(11):111119, 2006.

[28] Jens Limpert, Fabian Roeser, Damian N. Schimpf, Enrico Seise, Tino Eidam, Steffen Haedrich, Jan Rothhardt, Cesar Jauregui Misas, and Andreas Tuennermann. High Repetition Rate Gigawatt Peak Power Fiber Laser-Systems: Challenges, Design, and Experiment. *IEEE JOURNAL OF SELECTED TOPICS IN QUANTUM ELECTRONICS*, 15(1):159–169, JAN-FEB 2009.

[29] William S. Wong, Xiang Peng, Joseph M. McLaughlin, and Liang Dong. Breaking the limit of maximum effective area for robust single-mode propagation in optical fibers. *Opt. Lett.*, 30(21):2855–2857, 2005.

[30] Ingmar Hartl, H. A. McKay, A. A. Marcinkevičius, L. Dong, and M. E. Fermann. Multi-core leakage-channel fibers with up to 26000 um2combined effective mode-field area. In *Conference on Lasers and Electro-Optics/International Quantum Electronics Conference*, page CWD1. Optical Society of America, 2009.

[31] Liang Dong, Xiang Peng, and Jun Li. Leakage channel optical fibers with large effective area. *J. Opt. Soc. Am. B*, 24(8):1689–1697, 2007.

[32] Libin Fu, Andrius Marcinkevicius, Hugh A. McKay, Michiharu Ohta, Martin E. Fermann, and Liang Dong. All glass leakage channel fibers with fluorine-doped silica pump cladding. In *Conference on Lasers and Electro-Optics/International Quantum Electronics Conference*, page CThR4. Optical Society of America, 2009.

[33] Siddharth Ramachandran. Spatially structured light in optical fibers: Applications to high-power lasers. In *Advanced Solid-State Photonics*, page MD1. Optical Society of America, 2009.

[34] Almantas Galvanauskas, M Craig. Swan, and Chi-Hung Liu. Effectively single-mode large core passive and active fibers with chirally coupled-core structures. In *Conference on Lasers and Electro-Optics/Quantum Electronics and Laser Science Conference and Photonic Applications Systems Technologies*, page CMB1. Optical Society of America, 2008.

[35] Shenghong Huang, Cheng Zhu, Chi-Hung Liu, Xiuquan Ma, Craig Swan, and Almantas Galvanauskas. Power scaling of ccc fiber based lasers. In *Conference on Lasers and Electro-Optics/International Quantum Electronics Conference*, page CThGG1. Optical Society of America, 2009.

[36] T Hirooka and M Nakazawa. Parabolic pulse generation by use of a dispersion-decreasing fiber with normal group-velocity dispersion. *OPTICS LETTERS*, 29(5):498–500, MAR 1 2004.

[37] R. M. Atkins, P. J. Lemaire, T. Erdogan, and V. Mizrahi. Mechanisms of enhanced UV photosensitivity via hydrogen loading in germanosilicate glasses. Electronics Letters, 29:1234 1235, July 1993.

[38] A. Galvanauskas, A. Heaney, T. Erdogan, and D. Harter. Use of volume chirped bragg gratings for compact high-energy chirped pulse amplification circuits. In Lasers and Electro-Optics, 1998. CLEO 98. Technical Digest. Summaries of papers presented at the Conference on, San Francisco, CA, May 1998.

[39] S. Santran, M. Martinez-Rosas, L. Canioni, L. Sarger, L. N. Glebova, A. Tirpak, and L. B. Glebov. Nonlinear refractive index of photo-thermo-refractive glass. Optical Materials, 28(4):401 407, 2006.

[40] V. Smirnov, OptiGrate Internal Report, 2009.

[41] Kaai-Hsui Liao, Dissertation, University of Michigan, 2007.

[42] L. B. Glebov, L. N. Glebova, V. I. Smirnov, M. Dubinkskii, L. D. Merkle, Semyon Papernov, and Ansgar W. Schmid. Laser damage resistance of photo-thermo-refractive glass Bragg grating. 17th Annual Solid State and Diode Laser Technology Review, SSDLTR-2004 Technical Digest, pages Poster4, 2004.

[43] R. Kashyap. *Fiber Bragg Gratings.* Academic Press, New York, 1st edition (march 15, 1999) edition, 1999.

[44] Kim A. Winick. Effective-index method and coupled-mode theory for almost-periodic waveguide gratings: a comparison. *Appl. Opt.*, 31(6):757–764, 1992.

[45] H. A. Haus, Waves and Fields in Optoelectronics. Englewood Cliffs, NJ: Prentice-Hall, 1984.

[46] G. P. Agrawal and N. K. Dutta, Long-Wavelength Semiconductor Lasers. New York: Van Nostrand Reinhold, 1986.

[47] L. R. Brovelli and U. Keller, Simple analytical expressions for the reflectivity and the penetration depth of a Bragg mirror between arbitrary media, Opt. Commun., vol. 116, pp. 343350, May 1995.

[48] O. V. Belai, E. V. Podivilov, and D. A. Shapiro. Group delay in Bragg grating with linear chirp. *OPTICS COMMUNICATIONS*, 266(2):512–520, OCT 15 2006.

[49] H. Bateman, A. ErdelyiHigher Transcendental Functions, vol. 1, McGrow-Hill, New York, 1953.

[50] V. Gapontsev, D. Gapontsev, N. Platonov, O. Shkurikhin, V. Fomin, A. Mashkin, M. Abramov, and S. Ferin. 2 kw cw ytterbium fiber laser with record diffraction-limited brightness. Lasers and Electro-Optics Europe, 2005. CLEO/Europe. 2005 Conference on, pages 508-, June 2005.

[51] Kai-Chung Hou, Ming-Yuan Cheng, Almantas Galvanauskas, Doruk Engin, Rupak Changkakoti, and Pri Mamidipudi. Multi-mw peak power scaling of single-transverse mode pulses using 80-m core yb-doped lma fibers. In Advanced Solid-State Photonics, page MF5. Optical Society of America, 2006.

[52] Smirnov; Vadim I. Galvanauskas; Almantas Liao; Kai-Hsiu Glebov; Leonid B, Flecher; Emilie. Stretching and compression of laser pulses by means of high efficiency volume diffractive gratings with variable periods in photo-thermo-refractive glass, us patent, 2008.

[53] S. Ramachandran, J. W. Nicholson, S. Ghalmi, M. F. Yan, P. Wisk, E. Monberg, and F. V. Dimarcello. Light propagation with ultralarge modal areas in optical fibers. *Opt. Lett.*, 31(12):1797–1799, 2006.

[54] Guoqing Chang, Matthew Rever, Vadim Smirnov, Leonid Glebov, and Almantas Galvanauskas. Femtosecond yb-fiber chirped-pulse-amplification system based on chirped-volume bragg gratings. *Opt. Lett.*, 34(19):2952–2954, 2009.

[55] Kai-Hsiu Liao, Ming-Yuan Cheng, Emilie Flecher, Vadim I. Smirnov, Leonid B. Glebov, and Almantas Galvanauskas. Large-aperture chirped volume bragg grating based fiber cpa system. *Opt. Express*, 15(8):4876–4882, 2007.

[56] M. Rever, S. Huang, V. Smirnov, E. Rotari, I. Cohanoshi, S. Mokhov, L. Glebov, and A. Galvanauskas. 200w, 350fs fiber cpa system enabled by chirped-volume-bragg-gratings and chirally-coupled-core fiber technology. volume 7580, page 75800Y. SPIE, 2010.

[57] Smirnov; Vadim I. Efimov; Oleg M, Glebov; Leonid B. High efficiency volume diffractive elements in photo-thermo-refractive glass, 2000.

[58] Christophe Dorrer and Jake Bromage. Impact of high-frequency spectral phase modulation on the temporal profile of short optical pulses. *Opt. Express*, 16(5):3058–3068, 2008.

[59] Martin E. Fermann, Almantas Galvanauskas, and Gregg Sucha. *Ultrafast lasers: technology and applications.* Marcel Dekker, New York, 2003. xii, 784 p.

[60] Michael Sumetsky, Benjamin Eggleton, and C. de Sterke. Theory of group delay ripple generated by chirped fiber gratings. *Opt. Express*, 10(7):332–340, 2002.

[61] Leon Poladian. Understanding profile-induced group-delay ripple in bragg gratings. *Appl. Opt.*, 39(12):1920–1923, 2000.

[62] E. Flecher L. B. Glebov A. Galvanauskas Ming-Yuan Cheng, V. I. Smirnov. High average power and energy scalable fiber cpa at 1558-nm using chirped volume bragg grating pulse stretchers and compressors. volume 6102. SPIE, 2006.

[63] Guoqing Chang, Chi-Hung Liu, Kai-Hsiu Liao, Vadim Smirnov, Leon Glebov, and Almantas Galvanauskas. 50-w chirped-volume-bragg-grating based fiber cpa at 1055-nm. In *Conference on Lasers and Electro-Optics/Quantum Electronics and Laser Science Conference and Photonic Applications Systems Technologies*, page CMEE4. Optical Society of America, 2007.

[64] Guoqing Chang, Matthew Rever, Vadim Smirnov, Leon Glebov, and Almantas Galvanauskas. Femtosecond yb-fiber cpa system based on chirped-volume-bragg-gratings. In *Advanced Solid-State Photonics*, page MD4. Optical Society of America, 2008.

[65] Almantas Galvanauskas, Ming-Yuan Cheng, Kai-Chung Hou, and Kai-Hsiu Liao. High peak power pulse amplification in large-core Yb-doped fiber amplifiers. *IEEE JOURNAL OF SELECTED TOPICS IN QUANTUM ELECTRONICS*, 13(3):559–566, MAY-JUN 2007.